AGU ADVANCING EARTH AND SPACE SCIENCES

Space Weather®

RESEARCH ARTICLE
10.1029/2023SW003729

Solar Wind With Field Lines and Energetic Particles (SOFIE) Model: Application to Historical Solar Energetic Particle Events

Lulu Zhao[1], Igor Sokolov[1], Tamas Gombosi[1], David Lario[2], Kathryn Whitman[3,4], Zhenguang Huang[1], Gabor Toth[1], Ward Manchester[1], Bart van der Holst[1], Nishtha Sachdeva[1], and Weihao Liu[1]

[1]Department of Climate and Space Sciences and Engineering, University of Michigan, Ann Arbor, MI, USA, [2]NASA Goddard Space Flight Center, Greenbelt, MD, USA, [3]University of Houston, Houston, TX, USA, [4]KBR, Houston, TX, USA

Key Points:

- The >10 MeV energetic protons can be predicted using the physics-based model SOlar-wind with FIeld-lines and Energetic-particles (SOFIE)
- The background of the acceleration and transport processes of energetic protons are resolved using data driven magnetohydrodynamic model
- The default and free parameters of the SOFIE model are evaluated

Correspondence to:
L. Zhao,
zhlulu@umich.edu

Citation:
Zhao, L., Sokolov, I., Gombosi, T., Lario, D., Whitman, K., Huang, Z., et al. (2024). Solar wind with field lines and energetic particles (SOFIE) model: Application to historical solar energetic particle events. *Space Weather*, *22*, e2023SW003729. https://doi.org/10.1029/2023SW003729

Received 17 SEP 2023
Accepted 13 AUG 2024

Abstract In this paper, we demonstrate the applicability of the data-driven solar energetic particle (SEP) model, SOlar-wind with FIeld-lines and Energetic-particles (SOFIE), to simulate the acceleration and transport processes of SEPs and make forecast of the energetic proton flux at energies ≥10 MeV that will be observed near 1 AU. The SOFIE model is built upon the Space Weather Modeling Framework developed at the University of Michigan. In SOFIE, the background solar wind plasma in the solar corona and interplanetary space is calculated by the Stream-Aligned Aflvén Wave Solar-atmosphere Model(-Realtime) driven by the near-real-time hourly updated Global Oscillation Network Group solar magnetograms. In the background solar wind, coronal mass ejections (CMEs) are launched by placing an force-imbalanced magnetic flux rope on top of the parent active region, using the Eruptive Event Generator using Gibson-Low model. The acceleration and transport processes are modeled by the Multiple-Field-Line Advection Model for Particle Acceleration. In this work, nine SEP events (Solar Heliospheric and INterplanetary Environment challenge/campaign events) are modeled. The three modules in SOFIE are validated and evaluated by comparing with observations, including the steady-state background solar wind properties, the white-light image of the CMEs, and the flux of solar energetic protons, at energies of ≥10 MeV.

Plain Language Summary In this paper, we describe a physics-based solar energetic particle (SEP) model, called Solar-wind with FIeld-lines and Energetic-particles (SOFIE). This model is designed to simulate the acceleration and transport processes of SEPs in the solar atmosphere and interplanetary space. SOFIE is built on the Space Weather Modeling Framework developed at the University of Michigan. There are three modules in the SOFIE model, the background solar wind module, the coronal mass ejection (CME) initiation and propagation module, and the particle acceleration and transport module. The background solar wind plasma in the solar corona and interplanetary space is modeled by the Stream-Aligned Aflvén Wave Solar-atmosphere Model(-Realtime) driven by the near-real-time hourly updated Global Oscillation Network Group solar magnetograms. In the background solar wind, the CMEs are launched by placing an force-unbalanced magnetic flux rope on top of the active region, using the Eruptive Event Generator using Gibson-Low configuration. The acceleration and transport processes are then modeled by the Multiple-Field-Line Advection Model for Particle Acceleration. Using SOFIE, we modeled nine historical SEP events. The performance of the model and its capability in making space radiation prediction is discussed.

1. Introduction

Solar energetic particles (SEPs) can be accelerated over a wide range of energies extending up to GeVs. They are hazardous not only to humans in space but also to electronics and other sensitive components of spacecraft affecting their operations. Protons of >100 MeV with elevated fluxes exceeding 1 proton flux unit (pfu, #/cm^2/s/sr) are responsible for an increased astronaut exposure inside spacecraft shielding, and protons of >150 MeV are very difficult to shield against as they can penetrate 20 gm cm^{-2} (7.4 cm of Al, or 15.5 cm of water/human tissue) (e.g., Reames, 2013). Furthermore, >500 MeV protons can penetrate the atmosphere and pose radiation hazards to aviation. Besides protons, energetic heavy ions can also be of severe radiation concerns. Therefore, a reliable prediction of the timing and absolute flux of energetic particles above different energies is needed to provide

support for future space exploration. However, the sparsity and large variability of SEP events make them difficult to predict.

Many currently existing SEP prediction models use post-eruptive observations of solar flares/coronal mass ejection (CME)s to predict SEP events (e.g., Balch, 2008; Belov, 2009; Garcia, 2004; X. Huang et al., 2012; Inceoglu et al., 2018; Laurenza et al., 2009; Richardson et al., 2018; Smart & Shea, 1976, 1989, 1992). There are also models that make predictions of the eruptive events (flares, CMEs, SEPs) using solar magnetic field measurements (Anastasiadis et al., 2017; Bloomfield et al., 2012; Bobra & Couvidat, 2015; Bobra & Ilonidis, 2016; Boucheron et al., 2015; Colak & Qahwaji, 2009; Engell et al., 2017; Falconer et al., 2014; García-Rigo et al., 2016; Georgoulis, 2008; X. Huang et al., 2018; Kasapis et al., 2022; Papaioannou et al., 2015; Park et al., 2018; Tiwari et al., 2015). In addition, because of the shorter transit times of relativistic electrons or very high energy protons compared to ∼10 MeV protons, near-real-time observations of ∼MeV electrons (Posner, 2007) and/or >100 MeV protons (Boubrahimi et al., 2017; Nunez, 2011; Núñez, 2015) have also been used to predict the arrival of >10 MeV protons.

A recent review by Whitman et al. (2022) summarizes more than three dozen SEP models to predict the occurrence probability and/or properties of SEP events. In Whitman et al. (2022), three approaches of the prediction models are discussed: empirical, machine learning (ML) and physics-based models. Empirical and ML models are built upon potential causality relations between the observable and predictable and they can make rapid predictions, often within seconds or minutes after the input data becoming available. Such models hold value as they can generally issue forecasts prior to the peak of an SEP event. However, since empirical and ML models are built upon historic events, it is difficult to validate their predictions at locations where no routine/historical observations have been made, for example, the journey from Earth to Mars. And predictions can only be made for the specific energy channels upon which these models are built/trained. These models may also have difficulty in predicting extreme events since there are few such events available for training (e.g., Bain et al., 2021; Núñez, 2015; Whitman et al., 2022). On the other hand, physics-based models are based on first principles (Afanasiev et al., 2023; Alberti et al., 2017; Alho et al., 2019; Aran et al., 2017; Borovikov et al., 2018; Hu et al., 2017; Kozarev et al., 2017, 2022; Li et al., 2021; Linker et al., 2019; Luhmann et al., 2007; Marsh et al., 2015; Palmerio et al., 2024; Schwadron et al., 2010; Sokolov et al., 2004; Strauss & Fichtner, 2015; Tenishev et al., 2021; Wijsen et al., 2020, 2022; Zhang & Zhao, 2017). Physics-based models are usually computationally expensive, and in order for these models to make meaningful predictions, they need to run faster than real-time. Moreover, many of the underlying physical mechanisms involved in the development of SEP events are still under-debate, including the particle acceleration processes in the low corona, the particle's interaction with turbulence magnetic fields in the heliosphere, and the seed particles that are injected into the particle acceleration processes. However, physics-based models are still highly attractive, since they solve the acceleration and transport processes of energetic particles and therefore they are able to provide time profiles and energy spectra of SEPs at any location of interest in the heliosphere.

In this work, we demonstrate our attempt to model and make potential predictions of the energetic protons by using the physics-based model, called SOlar wind with FIeld lines and Energetic particles (SOFIE). We will apply the SOFIE model to nine historical SEP events chosen from the Solar Heliospheric and INterplanetary Environment (SHINE) challenge/campaign events, which were selected to challenge the SEP prediction models, based on their elevated intensities that were relevant to operations (https://ccmc.gsfc.nasa.gov/challenges/sep/shine2018/, https://ccmc.gsfc.nasa.gov/challenges/sep/shine2019/, https://ccmc.gsfc.nasa.gov/community-workshops/ccmc-sepval-2023/).

2. SOFIE

In order to build a physics-based SEP model, a background solar wind module, a CME generation and propagation module, and a particle acceleration and transport module are required. In SOFIE, the background solar wind plasma in the solar corona and interplanetary space is modeled by the Alfvén Wave Solar-atmosphere Model (-Realtime) (AWSoM-R) driven by hourly solar magnetograms obtained from the Global Oscillation Network Group (GONG) of the National Solar Observatory (NSO) (https://gong.nso.edu/data/magmap/). CMEs are launched by placing an imbalanced magnetic flux rope on top of the parent active region (AR), using the Eruptive Event Generator using Gibson-Low configuration (EEGGL). The propagation of the CME in the solar corona and interplanetary space is modeled by AWSoM-R. The acceleration and transport processes of energetic particles are

then modeled by the Multiple-Field-Line-Advection Model for Particle Acceleration (M-FLAMPA) (Borovikov et al., 2018; Sokolov et al., 2004). All the three modules are fully integrated through the Space Weather Modeling Framework (SWMF) developed at the University of Michigan. At the beginning of the simulation, magnetic field lines are extracted from the AWSoM-R solution by the M-FLAMPA module. The plasma properties of the grid points along the extracted magnetic field lines are obtained from the AWSoM-R solution. After the simulation begins, AWSoM-R and M-FLAMPA run concurrently. At each time step, the grid points along the magnetic field lines move with the corresponding velocity, and the plasma properties of the grid points are updated/extracted from AWSoM-R solution and passed to M-FLAMPA. The SOFIE model is built on the work by Borovikov et al. (2018), in which the three modules have been discussed in details. In this section, we briefly describe each module and the difference between SOFIE and the model in Borovikov et al. (2018).

2.1. Background Solar Wind

The 3D global solar wind plasma in the Solar Corona (1 solar radius (R_s) − 20 R_s) and inner heliosphere (20 R_s − 5 AU) is modeled by using AWSoM-R in the SWMF (Gombosi et al., 2018, 2021; Sokolov et al., 2013, 2021). AWSoM-R is an Aflvén wave-driven, self-consistent solar atmosphere model, in which the coronal plasma is heated by the dissipation of two discrete turbulence populations propagating parallel and antiparallel to the magnetic field (Sokolov et al., 2013). The AWSoM-R solar wind model has been validated by comparing simulations and observations of both the in-situ macroscopic properties of the solar wind and the line-of-sight (LoS) appearance of the corona observed in different wavelengths (Sachdeva et al., 2019, 2021). The inner boundary of AWSoM-R is characterized by the magnetic field measurement made by either ground-based or space-based observatories. In all the SEP events we modeled in this work, hourly-updated GONG solar magnetograms are used (https://gong.nso.edu/data/magmap/).

A validated background solar wind solution is critical in modeling the transport processes of energetic particles as it provides the magnetic field configuration where particles propagate, allowing the computation of the energetic particle properties observed by spacecraft at specific heliospheric locations. Numerical solutions of the full set of ideal or resistive magnetohydrodynamic (MHD) equations so far have not been able to reproduce aligned interplanetary stream lines and magnetic field lines in corotating frames. One of the reasons for this discrepancy is the numerical reconnection across the heliospheric current sheet: the reconnected field is directed across the current sheet, while the global solar wind streams along the current sheet, thus resulting in “V-shaped” magnetic field lines and significant misalignment between field lines and stream lines. It is unfeasible to follow particles' trajectory in “V-shaped” magnetic field lines, therefore, stream lines are usually used instead (Young et al., 2020). Within regular MHD, there is no mechanism to re-establish the streamline-field line alignment. Recently, Sokolov et al. (2022) introduced the Stream-Aligned MHD method that “nudges” the magnetic field lines and plasma stream lines toward each other. A detailed explanation and illustration of this method is discussed in Sokolov et al. (2022). In SOFIE, in contrast to Borovikov et al. (2018), we solve Stream-Aligned MHD to get a steady state solar wind plasma background representative of the pre-event ambient solar wind and magnetic medium where CMEs and SEPs propagate.

2.2. CME Generation and Propagation

The CME generation in SOFIE is modeled by the EEGGL module in SWMF (Borovikov et al., 2017; Jin et al., 2016, 2017a, 2017b; Kataoka et al., 2009; Lugaz et al., 2005, 2007; Manchester, Gombosi, Roussev, Ridley, et al., 2004; Manchester, Gombosi, Roussev, Zeeuw, et al., 2004; Manchester et al., 2006; Manchester, Kozyra, et al., 2014; Manchester, van der Holst, & Lavraud, 2014; Shiota & Kataoka, 2016). The initial conditions of the CME within the solar corona is treated by inserting an unstable (or force imbalanced) flux rope suggested by Gibson and Low (1998) into an AR. The magnetogram from GONG and the observed CME speed (from Coordinated Data Analysis Web (CDAW) catalog, https://cdaw.gsfc.nasa.gov/CME_list/ and/or The Space Weather Database Of Notifications, Knowledge, Information (DONKI) database, https://kauai.ccmc.gsfc.nasa.gov/DONKI/) are used to calculate the flux rope parameters. This approach offers a relatively simple, and inexpensive model for CME initiation based on empirical features of pre-event conditions (e.g., Jin et al., 2017a, 2017b). The EEGGL module is publicly available for download at https://github.com/SWMFsoftware or can also be used through the website of the Community Coordinated Modeling Center (CCMC, https://ccmc.gsfc.nasa.gov/eeggl/). The subsequent propagation of CMEs in the solar corona and interplanetary medium are modeled using the AWSoM-R module. The use of EEGGL model to initialize CMEs and the subsequent CME/ICME evolution has

Table 1
Observational Facts of the Nine Solar Energetic Particle Events

Event date	CME onset time[a] (UT)	CME speed[b] (km/s)	SXR GOES flare class/onset (UT)	NOAA AR
7 March 2012	7 March 2012 00:24	2,040	X5.4/00:02	N17E15 (11429)
17 May 2012	17 May 2012 01:37	1,263	M5.1/01:25	N12W89 (11476)
12 July 2012	12 July 2012 16:54	1,400	X1.4/15:37	S14W02 (11520)
11 April 2013	11 April 2013 07:24	743	M6.5/06:55	N09E12 (11719)
7 January 2014	7 January 2014 18:12	2,048	X1.2/18:04	S15W11 (11943)
14 July 2017	14 July 2017 01:25	750	M2.4/01:07	S09W33 (12665)
4 September 2017	4 September 2017 20:24	1,323	M5.5/20:12[c]	S08W16 (12673)
6 September 2017	6 September 2017 12:12	1,816	X9.3/11:53	S08W34 (12673)
10 September 2017	10 September 2017 15:48	2,087	X8.2/15:35	S08W88 (12673)

[a]The onset time is obtained from the Solar Heliospheric and INterplanetary Environment (SHINE) challenge websites and visually examined to match the Solar and Heliospheric Observatory observations. [b]The coronal mass ejection (CME) speed is provided by the SHINE challenge website. [c]Based on inspection of SDO/AIA images.

been extensively studied and validated (e.g., Jin et al., 2017a, 2017b; Manchester, Gombosi, Roussev, Ridley, et al., 2004; Manchester et al., 2005, 2008, 2012; Manchester & van der Holst, 2017; Manchester, van der Holst, & Lavraud, 2014; Roussev, 2008; Roussev et al., 2004; van der Holst et al., 2007, 2009).

2.3. Particle Tracker

In SOFIE, protons are accelerated at the shocks driven by CMEs through first order Fermi acceleration mechanism (Axford et al., 1977; Bell, 1978a, 1978b; Blandford & Ostriker, 1978; Krymsky, 1977). The acceleration and transport processes are modeled by the M-FLAMPA module in SWMF. In M-FLAMPA, the time-evolving magnetic field lines are extracted from the AWSoM-R solutions, along which the particle distribution functions are solved, following the Parker diffusion equation (Borovikov et al., 2018; Sokolov et al., 2004). Novel mathematical methods are applied to the extracted magnetic field lines to sharpen the shocks thus making the Fermi acceleration process more efficient (Sokolov et al., 2004). The injection of suprathermal protons into the CME-driven shock acceleration system is described in Sokolov et al. (2004). The interaction between the energetic protons and turbulent magnetic fields is modeled by the diffusion processes along the background magnetic field lines. The diffusion coefficient close to the shock region is calculated through the total Aflvén wave intensities obtained in the MHD simulation, and a Kolmogorov spectrum with an index of −5/3 is assumed. The diffusion coefficient upstream of the shock is calculated by assuming a constant mean free path (mfp). Detailed parameter settings will be discussed in Section 4.

3. Overview of the Nine SEP Events

The nine SHINE challenge events were primarily chosen because they were large SEP events that were relevant to operations. Specifically, the 12 July 2012 event was selected because there was a large particle enhancement at Mars. In this section, we describe the observational facts of the nine SEP events. Table 1 summarizes the observational facts of the CMEs and solar flares associated with the solar origin of the nine events. From left to right, each column shows the SEP event date used to identify the event, the associated CME onset time, the CME speed, the soft X-ray flare class and onset time, the National Oceanic and Atmospheric Administration (NOAA) AR locations on the Sun, and the NOAA AR number. The CME onset time is estimated from observations made by the Large Angle and Spectrometric Coronagraph (LASCO) instrument on board Solar and Heliospheric Observatory (SOHO) (Brueckner et al., 1995). Note that all the CMEs associated with the SEP events modeled in this work are categorized as halo CME in the SOHO LASCO CME catalog CDAW (https://cdaw.gsfc.nasa.gov/CME_list/halo/halo.html). Each individual SEP event has been studied extensively by many papers as described below. Key features of each individual event are as follows:

3.1. 7 March 2012 Event

The solar origin of this SEP event is temporally associated with a X5.4 class X-ray flare from the NOAA AR 11429 at N17E15. At 00:24 UT, a fast halo CME with a plane-of-sky speed of 2,040 km s^{-1} was detected in LASCO/C2 coronagraph images. At 01:05 UT, a second flare with a class of X1.3 erupted from the same AR and a slower halo CME with a speed of 1,825 km s^{-1} was detected. Detailed analyses of these two eruptions can be found elsewhere (e.g., Patsourakos et al., 2016). The fact that the first CME was faster than the second CME and that the electron intensities measured by the MErcury Surface, Space ENvironment, GEochemistry, and Ranging (MESSENGER) at 0.31 AU peaked before the occurrence of the second flare (cf. Figure 6 in Lario et al., 2013) suggest that the main contributor to the observed SEP event was the first solar eruption. In fact, in the analysis of SEP events observed by the two spacecraft of the Solar Terrestrial Relations Observatory (i.e., Solar TErrestrial RElations Observatory (STEREO)-Ahead and STEREO-Behind) and near-Earth spacecraft, Richardson et al. (2014) and Kouloumvakos et al. (2016) concluded that the first flare/CME was responsible for the SEP event at all three locations. Therefore, in the simulation, we will consider only the first CME. Yet the energetic particle measurement made by Geostationary Operational Environmental Satellite (GOES) shows two clear onset phases, which may correspond to the two CMEs. The peak and decay phases of the intensity profile was indistinguishable.

3.2. 17 May 2012 Event

This event was the first Ground Level Enhancement (GLE) of solar cycle 24 with >433 MeV proton intensity enhancements detected by GOES-13 and up to $\gtrsim$7 GeV as inferred from neutron monitor observations (Balabin et al., 2013; Li et al., 2013). This GLE, designated as GLE71, had the peculiarity of having a highly anisotropic onset as detected by several neutron monitor stations (Mishev et al., 2014). By assuming that relativistic protons propagated scatter-free along nominal interplanetary field lines, Li et al. (2013) estimated that ~1.12 GeV protons were release at about 01:39 ± 00:02 UT, in accordance with a type II radio burst and prominence eruption at the origin of the associated fast CME, and corresponding to a height of the CME at ~3.07 R_s. It is worth noting that Shen et al. (2013) reported two CME eruptions from the same AR that were separated by about 2 min. However, in the time intensity profiles of energetic protons detected by GOES, the two eruptions were not well separated. In this work, we will only consider the first CME eruption as the main accelerators of energetic particles. The same approach was adopted by Li et al. (2021) who modeled this event using AWSoM and improved Particle Acceleration and Transport in the Heliosphere model (iPATH) models.

3.3. 12 July 2012 Event

The CME at the origin of this SEP event generated the fourth strongest geomagnetic storm of solar cycle 24 (Gil et al., 2020). The prompt component of this SEP event showed >100 MeV proton intensity enhancements as observed by GOES-13 (cf. Figure 6 in Gil et al., 2020) and the arrival of the shock at 1 AU driven by the CME was accompanied by a strong energetic storm particle event (e.g., Wijsen et al., 2022). Details of the solar eruption that generated this event, reconstructions of the CME structure as observed by coronagraphs, and the topology of the CME at its arrival at 1 AU can be found in Scolini et al. (2019), Gil et al. (2020), and references therein.

3.4. 11 April 2013 Event

This SEP event was the first Fe-rich event of solar cycle 24 as evidenced by ion data collected by STEREO-B and near-Earth spacecraft (Cohen et al., 2014). The filament eruption origin of the CME that generated this SEP event has been studied by several authors (e.g., Fulara et al., 2019; Joshi et al., 2017; Vemareddy & Mishra, 2015). The EUV wave associated with the origin of this event propagated mostly toward the footpoint of the nominal interplanetary magnetic field line connecting to STEREO-B, but signatures of the EUV wave reaching the footpoints of the interplanetary magnetic field lines connecting to either STEREO-A or near-Earth spacecraft were not observed (Lario et al., 2014). The non-arrival of the EUV wave at the magnetic footpoint of a given spacecraft does not preclude the observation of SEPs by such a spacecraft. Lario et al. (2013) concluded that observation of particles by near-Earth spacecraft was due to the CME-driven shock expanding at higher altitudes over a wide range of longitudes, without leaving an observable EUV trace in the low corona, being able to accelerate and inject particles onto the field lines connecting to near-Earth locations.

3.5. 7 January 2014 Event

The solar eruption at the origin of the CME associated with the SEP event was analyzed in detail by Möstl et al. (2015). They showed that the CME was "channeled" by strong nearby AR magnetic fields and open coronal fields into a non-radial propagation direction within ~2.1 R_S, in contrast to deflection in interplanetary space. This phenomenon will be discussed in more detailed in Section 4, where a white-light coronagraph comparison between the simulation and observation is discussed. Mays et al. (2015) studied the propagation of this CME up to 1 AU and determined that only a glancing CME arrival was observed at Earth. The SEP intensity enhancement occurred on the tail of a very energetic SEP event with onset on 6 January 2014 (see details in, e.g., Kühl et al., 2015; Thakur et al., 2014).

3.6. 14 July 2017 Event

The origin of this event was associated with a medium-sized (M2.4) long-duration (almost 2 hr) flare from a large AR that displayed a sigmoidal configuration associated with a filament/flux rope. A high-lying coronal EUV loop was seen moving outward, which was immediately followed by the impulsive phase of the flare (Jing et al., 2021). The formation of the sigmoidal filament/flux rope, its expansion, and the evolution of the photospheric magnetic field, leading to the eruption of the filament and the resulting CME have been studied in detail by James et al. (2020) (see their Figure 13). The arrival of the shock at Earth, accompanied by local particle intensity increases at energies $\lesssim$10 MeV, generated a geomagnetic storm $K_p = 6$.

3.7. 4 September 2017 Event

This SEP event, together with the following two SEP events, are a series of SEP events that occurred in early September 2017, toward the end of solar cycle 24. The solar eruptions associated with the origin of these events and their geomagnetic effects were analyzed by Chertok et al. (2018) and Shen et al. (2018) and references therein, whereas the resulting SEP events were described by Bruno et al. (2019) among others. The flare associated with the first SEP event occurred at 20:12 UT on 4 September 2017 and the CME occurred at 20:24 UT with a speed of 1,323 km s^{-1}. The active region (AR 12673) was located at S09W16. The flare onset time was estimated from the SDO/AIA movies. From SOHO/LASCO C2 images, around two hours before the eruption of the CME associated with the SEP event, there was a preceding CME at 18:48 UT on 4 September 2017 with a speed of 597 km s^{-1} (CDAW). From the view of SOHO/LASCO, the first CME propagates to the west whereas the second faster CME propagates toward the southwest. The second CME overtook the previous CME shortly after its eruption, around 21:24 UT. In this work, we attribute the main acceleration of protons to the second CME, which is faster and stronger.

3.8. 6 September 2017 Event

A X9.3 class flare occurred at 11:54 UT on 6 September 2017 from the same AR AR 12673 as the 4 September 2017 event. At this time, the AR was located at S08W34. The CME has a speed of 1,816 km s^{-1}. The occurrence of this SEP event was in the decay phase of the previous event, making the identification of the onset of the energetic proton intensity enhancements at different energies difficult.

3.9. 10 September 2017 Event

At 15:35 UT on 10 September 2017, the same AR AR 12673 produced a X8.2 class flare. The AR rotated to S08W88. The corresponding CME has a speed of 2,087 km s^{-1}. This event is an GLE event, GLE #72. This event was also well-studied by multiple groups (see details in Z. Ding et al., 2020; Zhu et al., 2021).

4. SOFIE Results

In this section, we present the results of the SOFIE model in simulating the nine SEP events. When modeling each event, we first run the AWSoM-R model to get a steady state solution of the background solar wind. In doing so, the hourly GONG magnetogram measured right before the flare eruption is chosen to drive the AWSoM-R model. The simulation domain extends from 1.105 R_s to 2.5 AU. In Section 4.1, we discuss the background solar wind solutions for each event and compare them with in-situ observations made by near-Earth instruments. After getting the steady state solar wind solution, an imbalanced magnetic flux rope is placed on top of the AR where the

CME erupted from. In Section 4.2, we show the 3D topology of the magnetic flux rope and compare the white-light coronagraph images calculated from simulation with the LASCO/C2 observations. In Section 4.3, we show the 2D spatial distribution of energetic particles in a sphere around Earth and the extracted proton flux time profiles.

4.1. Background Solar Wind

In Figure 1, the macroscopic properties of the background solar wind for the nine SEP events are shown. For each event, a total time period of 27 days is shown, corresponding approximately to the synodic solar rotation period. In this paper, we only show the in-situ properties of the solar wind and its validation against the observation. The validation of the AWSoM(-R) model using the predicted LoS appearance of the corona in different wavelengths has been discussed in detail in Sachdeva et al. (2019) and Gombosi et al. (2021).

In each panel of Figure 1, the solar wind properties including the radial bulk plasma speed (U_r), the proton number density (N_p), the temperature, and the total magnetic field magnitude (B) are plotted from top to bottom. The simulation results are plotted in red and the observations, measured by the Advanced Composition Explorer (ACE), are plotted in black. The time period corresponding to the passage of the ICME are plotted in shaded teal. The ICME time periods are obtained from the list of ICMEs observed at 1 AU (https://izw1.caltech.edu/ACE/ASC/DATA/level3/icmetable2.htm) (Cane & Richardson, 2003; Richardson & Cane, 2010). Since we solve the steady state background solar wind, the ICME structures, which are the counterparts of the CMEs in interplanetary space, are not modeled and will not be compared. Most of the SEP events occur in solar maximum, especially the ones that we model in this work. Therefore, in multiple panels of Figure 1, one can see more than one ICME in the observations. As we mentioned above, the ICMEs in the observations will not be captured by the simulation. The mismatch between the simulation and observation in the ICME time period is expected. One of the factors that can lead to the mismatch between the observation and simulation in the quiet solar wind period is the magnetogram that we used to drive the MHD simulation. Previous studies have suggested that the simulated solar wind for the same time interval can be different if different magnetograms are used (Gressl et al., 2014; Jin et al., 2022). Z. Huang et al. (2024) compared the simulated solar wind using ADAPT-GONG and GONG magnetograms and found that ADAPT-GONG magnetograms can provide better 1 AU solar wind prediction, except for solar maximum conditions. In this work, we chose the GONG magnetogram, because GONG magnetogram is recommended for operational use based on private communication with the space weather prediction center at NOAA. In this work, we used the mangetogram that was obtained right before the eruption of the parent flare. Therefore, the plasma properties calculated from the simulation may not compare well with the real observation. More factors that may lead to the mismatch between observation and simulation can be found in Sachdeva et al. (2019) and Z. Huang et al. (2023).

When running the AWSoM-R model, to get a reasonable comparison between the simulations and observations, there are two important adjustable input parameters: the Poynting flux parameter and the correlation length of the Alfvén wave dissipation (see details in Z. Huang et al., 2023; Jivani et al., 2023; van der Holst et al., 2014). The Poynting flux parameter determines the input energy at the inner boundary to heat the solar corona and accelerate the solar wind, and the correlation length describes the dissipation of Alfvén wave turbulence in the solar corona and heliosphere (Z. Huang et al., 2023). The best simulated solar wind background was determined by minimizing the curve differences between the observation and simulation for the solar wind density, velocity and magnetic field, as they are critical for the CME propagation and SEP transport. The curve distances between the simulation and observation were calculated based on the formula suggested in Sachdeva et al. (2019). For all the nine background solar wind simulations in this work, the Poynting flux is the most critical parameter, among all the adjustable parameters. Therefore, when SOFIE will be used as the SEP prediction tool, the range of the "optimal" Poynting flux parameter will be determined based on the empirical formulas suggested in Z. Huang et al. (2023, 2024).

4.2. CMEs

After obtaining the steady state background solar wind solution, we then launch the CME from the location of the parent AR by placing an imbalanced Gibson-Low (Gibson & Low, 1998) magnetic flux rope. The parameters of the flux rope, including the total magnetic field, the flux rope size, and the flux rope orientation, are calculated based on the hourly GONG magnetogram and the observed CME speed. In Figures 2–4, we show the 3D topology

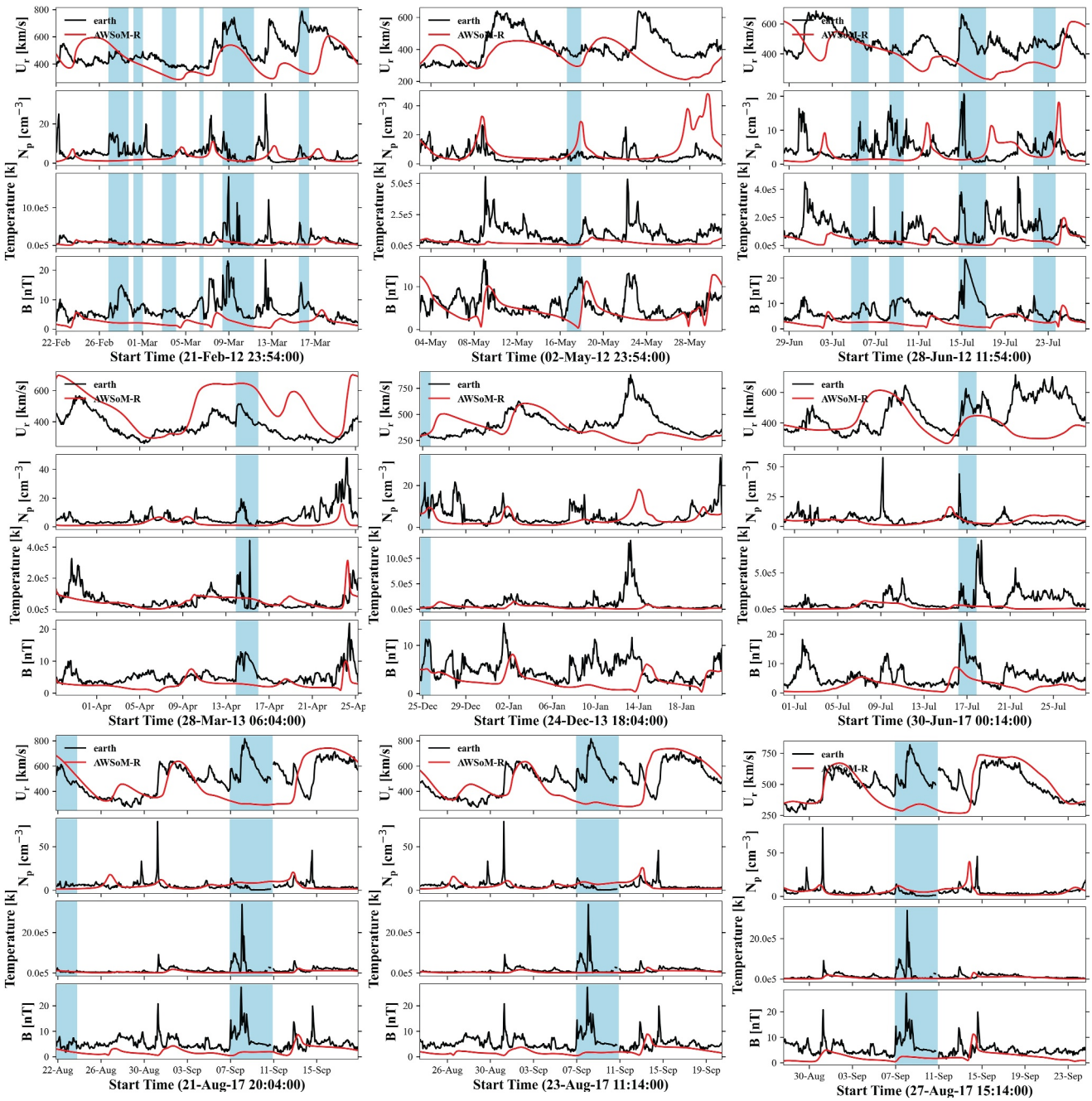

Figure 1. Macroscopic properties of the background solar wind for the nine solar energetic particle events. In each panel, the radial solar wind plasma speed, the solar wind density, the temperature, and the magnitude of the total magnetic field is shown from the top to bottom respectively. The simulation results from Aflvén Wave Solar-atmosphere Model(-Realtime) are plotted in red and observations are plotted in black. The passage of the ICME structures are shaded in teal.

of the inserted flux rope (left column), the white-light image measured by the LASCO/C2 coronagraph (middle column), and the synthetic white-light image calculated from the simulation (right column). The synthetic coronagraph images are created by integrating the Thomson-scattered light along the lines-of-sight that comprise the image. The number and distribution of lines are chosen to match the instrument of comparison, in this case LASCO/C2. We show total brightness images, which are the sum of the plane-of-sky and LoS polarization along with dust-scattered light. The original application is described by Manchester, Gombosi, Roussev, Ridley, et al. (2004). In the left column, the surface of the Sun (at 1.105 R_s) and a number of 3D magnetic field lines are colored according to the radial component of the magnetic field. Note that the Sun and the magnetic field lines do

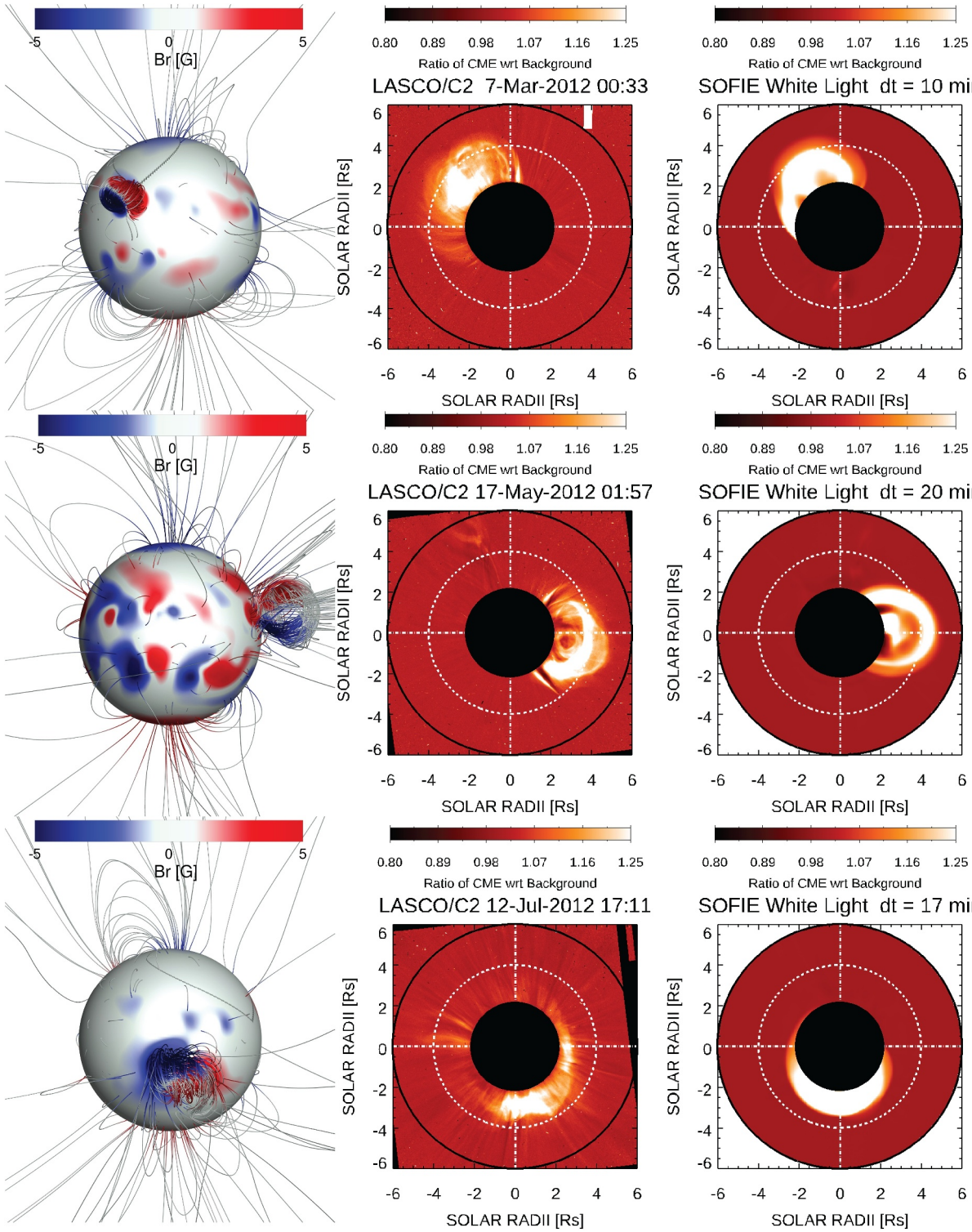

Figure 2. (left) The 3D topology of the inserted magnetic flux rope in the active region. (Middle) LASCO/C2 white-light image of the solar corona. (right) White-light image calculated from the simulation at the same time as shown in the middle column. In each of the white light images, the radius of the black solid circle, the white dashed circle, the black circle are 2.2 R_s, 4 R_s, and 6 R_s. Three events are shown here, 7 March 2012, 17 May 2012, and 12 July 2012. In the left column, the surface of the Sun (1.105 R_s) and the 3D magnetic field lines are colored with the radial magnetic field. The color bar shown in the plot presents the strength of the radial magnetic field in the field lines. The radial magnetic field on the Sun ranges from −20 to 20 G (color bar not shown here).

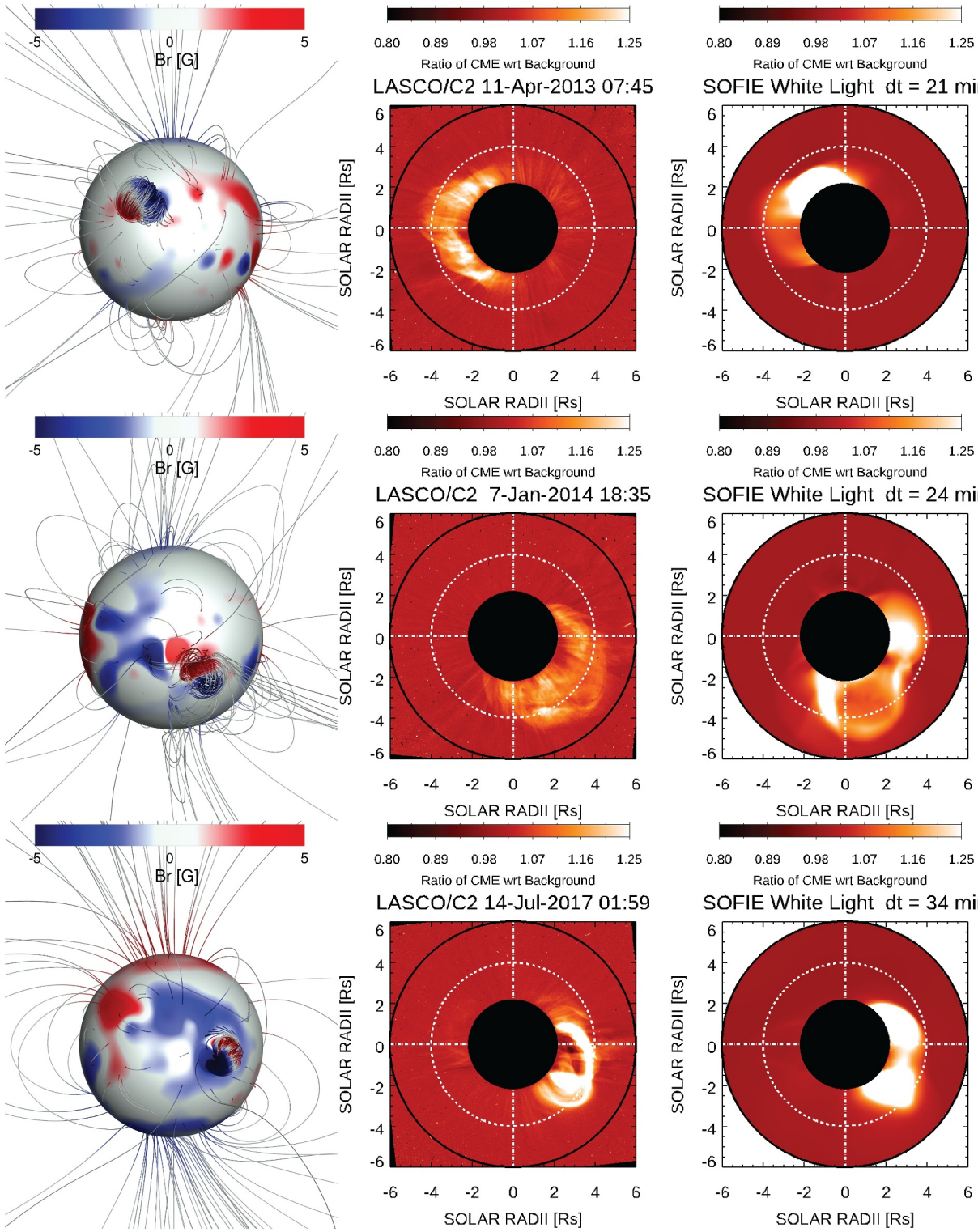

Figure 3. In the same format as Figure 2 for the three events 11 April 2013, 7 January 2014, and 14 July 2017.

not share the same color bar. The color bar shown in each plot represents the magnetic field strength along the magnetic field lines. The radial magnetic field on the Sun (at 1.105 R_s) ranges from −20 G to 20 G. The large-scale magnetic field lines, besides the flux rope, are plotted to represent the overall structures of the coronal magnetic fields in each event. It is clearly seen that the field configurations differ dramatically from event to

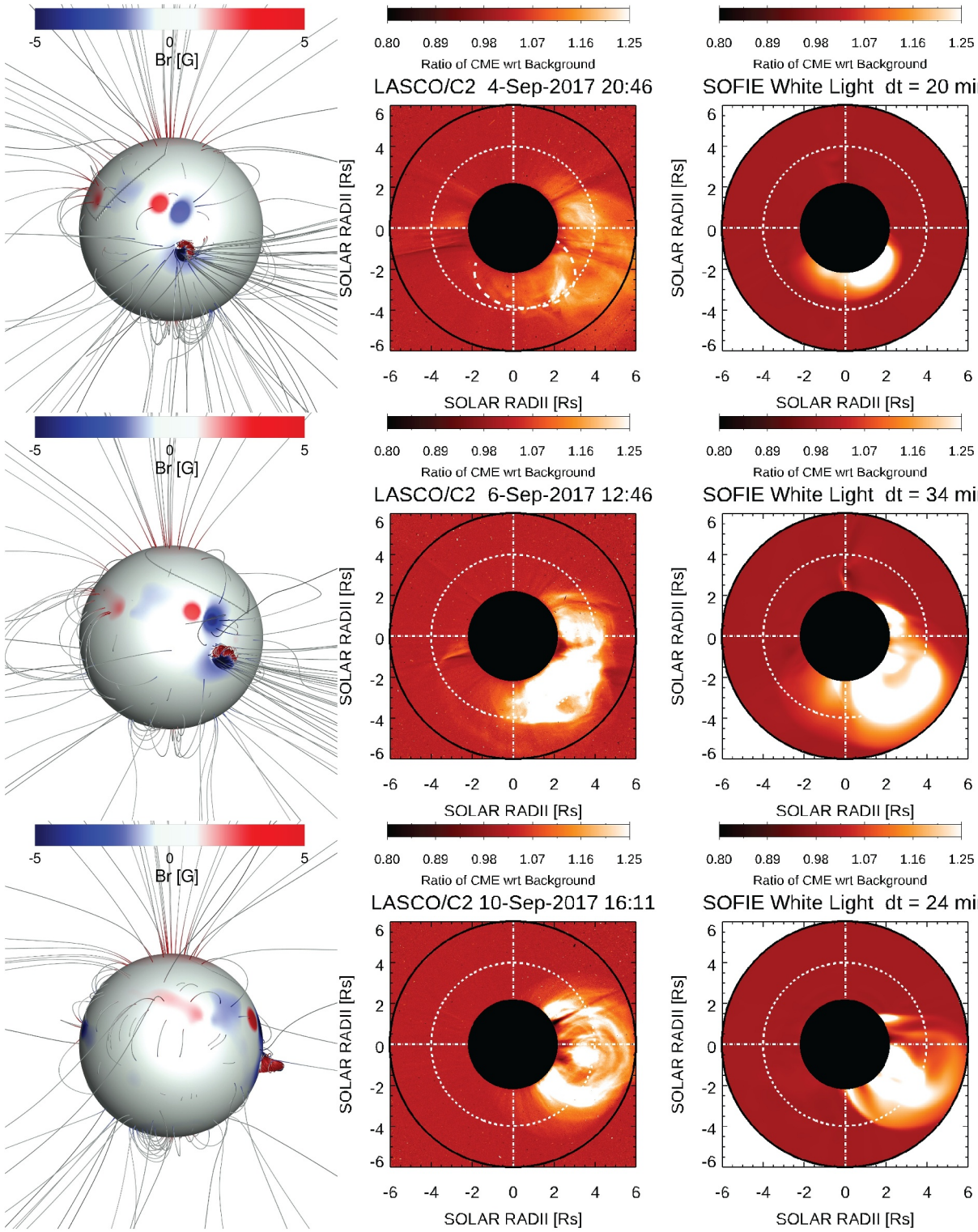

Figure 4. In the same format as Figure 2 for the three events 4 September 2017, 6 September 2017, and 10 September 2017.

event. And the overall magnetic field strength on the solar surface also varies by orders of magnitude. The perspective view of the Sun is that obtained from Earth. Therefore, due to projection effects, the flux rope of some events are not as distinguishable as the others, especially when the flux rope is located close to the center of the Sun, as viewed from Earth.

The middle and right columns of Figures 2–4 compare the white-light coronagraph observations (middle) and simulations (right) several tens of minutes after the eruption of each CME. The exact times shown in Figures 2–4 are selected on the basis of their clear CME detection in the LASCO/C2 field of view. The exact time of the selected observational frame is shown in the title of each image. The images calculated from the simulation are chosen accordingly and the time, *dt*, after the CME eruption is shown. In each of the white light images of Figures 2–4, the radius of the black solid circle, the white dashed circle, and the black circle are 2.2 R_s, 4 R_s, and 6 R_s.

In the rest of this section, we briefly describe the white-light comparison of each individual CME between the observation and simulation. In the 7 March 2012 event (top row of Figure 2), the core structure of the CME compares well, and the leading edge of the CME reaches approximately the same radial distance between observation and simulation, although the overall expansion of the CME in the simulation is narrower than the observation, especially in the left flank. In the 17 May 2012 event (middle row of Figure 2), the core structure, the leading edge, and the overall expansion of the CME are well-captured by the simulation. In the 12 July 2012 event (bottom row of Figure 2), the CME is a halo CME (CDAW) and the flux rope originated from the center of the Sun as seen from Earth (left column). Therefore, the projection effect is large. From the LASCO/C2 image (middle column), the core structure of the CME has a southern part (the AR is located at S14W02), which is captured in the simulation.

In the 11 April 2013 event (top row of Figure 3), the core structure of the CME propagates toward the east as seen in the LASCO/C2 images. The envelope of the CME appears to be symmetric with respect to the solar equator. However, in the white-light image obtained from the simulation, the northern part of the CME is brighter than the southern part, demonstrating an extreme asymmetric shape. We examined the plasma properties in the low solar corona and found a high density region lying in front of the flux rope which slowed down the propagation of the CME and led to such an asymmetric structure.

In the 7 January 2014 event (middle row of Figure 3), the CME erupted from the AR located at S15W11. From the LASCO/C2 point of view, the CME was a halo CME but propagating mostly in the southwest direction. The initial simulation also shows a halo CME (not shown here), which does not have the southwestern part as seen from the LASCO/C2 images. Therefore, it is very likely that the CME was deflected toward the west in the very early stage. We examined the magnetic fields around the AR where the flux rope was inserted and found there was a strong AR in the east of the flux rope. The CME eruption and propagation in this event has been analyzed in detail by Möstl et al. (2015). They found the CME was "channeled" by strong nearby AR magnetic fields and open coronal fields into a non-radial propagation direction within ∼2.1 R_s. In the current setup of simulations, since the initial speed of the CME was 2,048 km s^{-1}, the flux rope is difficult to be deflected in the early stage. Therefore, in order to match that of the LASCO/C2 observation and also match the subsequent propagation of the CME, we shifted the location of the flux rope to the adjacent AR in the west, separated by 8° in longitude from the AR listed in Table 1. As seen from Figure 3, the simulated CME propagates toward southwestern, which is comparable to the observations. However, the shifting of the flux rope to the west leads to issues when modeling the particle acceleration and propagation.

In the 14 July 2017 event (bottom row of Figure 3), the white-light image from the observation and simulation is comparable, except that the CME shows a bright northern part in the simulation. While in the observation, the core part of the CME leans toward the south. The 4 September 2017 event (top row of Figure 4) involved two CMEs. From the LASCO/C2 movie, there was a preceding CME eruption that occurred around 2 hr before the main CME, with a speed of 597 km s^{-1} (CDAW). The preceding CME propagated toward the west and the main CME took over the preceding CME shortly after the eruption. In the LASCO/C2 image (top row of Figure 4), we enclose the leading edge of the main CME for a better vision comparison with the simulation. In the simulation, we only launch the main CME. The radial distance of the CME leading edge and its propagation direction is in good agreement with the observation. Both the 6 September 2017 and 10 September 2017 events (middle and bottom rows of Figure 4) show very good agreement between simulations and observations, in terms of the CME speed and propagation direction, including the interaction of the flux rope with the high density streamers in the background solar wind.

4.3. Energetic Particles

Once the force-imbalanced flux rope was inserted into the AR, we run the coupled AWSoM-R and M-FLAMPA modules to solve the energetic particle acceleration and transport processes in the solar corona and inner

heliosphere. More than 600 magnetic field lines are extracted from the 3D AWSoM-R solution. The extracted magnetic field lines are followed in the local Lagrangian reference frame advecting with the solar wind plasma. A frequent (120 s) dynamic coupling between AWSoM-R and M-FLAMPA is performed to account for the propagation of the CME and CME-driven shock wave. In the simulation, the shock is identified by the sudden jump of the solar wind speed along the extracted magnetic field lines. A minimum and maximum jump ratio of the solar wind speed cross the shock is set to be 1.01 and 4.0. On each individual magnetic field line, the Parker diffusion equation is solved in the time-evolving Lagrangian coordinates. The diffusion strength close to the shock is determined by the total Aflvén wave intensity calculated from the AWSoM-R simulation. The diffusion mfp upstream of the shock, as described in Sokolov et al. (2004), is assumed to be a constant value, 0.3 AU for 10 MeV proton at 1 AU. The 0.3 AU is obtained through quasi linear theory (e.g., Jokipii, 1966), by assuming a magnetic field turbulence strength (dB^2) of 0.05 nT^2 and a total magnetic field of 1 nT at 1 AU. The effects of the mfp on the decaying phase of the SEP event has been well-studied by several studies (e.g., Kecskeméty et al., 2009; Zhao et al., 2016). We are aware of the change of the mfp may lead to different results, but in this work, to test the robustness of SOFIE, we adopt the single mfp across all events. And perpendicular diffusion due to the field line random walk is not modeled. In modeling the nine SEP events, we followed 648 magnetic field lines that cover 360° in longitude and −45° to 45° in latitude of the solar surface. The starting radial distance of the magnetic field lines is 2.5 R_s, and the magnetic field lines are traced inward and outward until reaching the inner and outer boundaries. The starting points of the magnetic field lines are chosen to distribute uniformly on the sphere at 2.5 R_s. The latitudes of the AR that we insert the flux rope are within ±17° of the solar equator. Therefore, a ±45° coverage in latitudes is sufficient to calculate the particle flux in the ecliptic plane.

When applying the diffusive shock acceleration (DSA) theory to particle accelerations at the moving shock, there is the so-called "Injection Problem" (e.g., Drury, 1983). In the DSA theory, a nearly isotropic pitch angle distribution of the injected particles is assumed. Therefore, the DSA theory cannot address the acceleration of thermal particles, because thermal particles are highly anisotropic in the shock frame. The "Injection Problem" has been well discussed in previous studies (e.g., Giacalone, 2003; Giacalone, 2005a, 2005b; Giacalone & Kóta, 2006; Guo et al., 2021). In this work, we are not trying to solve the "Injection Problem," instead, we set the injection energy, E_i, in the shock system to be 10 keV, above the thermal energies. And the injection energy is assumed to be the same at any location of the shock front (e.g., Giacalone & Kóta, 2006). The absolute level of the injected particles is determined by assuming a suprathermal tail ($\sim p^{-5}$) extending from the thermal momentum ($\sqrt{2mT}$) to the injected momentum (p_i) as follows (Sokolov et al., 2004):

$$f(p_i) = \frac{c_i}{2\pi} \frac{n}{(2mT)^{3/2}} \left(\frac{\sqrt{2mT}}{p_i} \right)^5 \tag{1}$$

where m is the proton mass, n and T are the local plasma density and temperature in energy units (if in Kelvins, $k_B T$ should stand instead, k_B being the Boltzmann constant) calculated from AWSoM-R simulation. c_i is the injection coefficient and p_i is the injection momentum. The suprathermal tail ($\sim p^{-5}$) is assumed to nearly follow the spectral shape of suprathermal tails usually observed in the solar wind (e.g., Fisk & Gloeckler, 2007, and reference therein). The physical meaning of the injection coefficient may be derived by integrating the assumed distribution of the suprathermal particles over momentum, which gives us their density: $4\pi \int_{\sqrt{2mT}}^{p_i} f p^2 \mathrm{d}p = c_i n$. Hence, c_i is a fraction of density of protons having suprathermal energy. The injection level for each individual event was assumed to be 1 when we did the simulations. In order to compare with the observations in the figures, the calculated proton flux is scaled up or down by a scaling factor to match with the observations at energies >10 MeV, for each individual event. Since the self-generated waves by the streaming proton are not calculated in the simulation, the acceleration and transport of protons are not affected by such scaling. The scaling factors can be understood as the difference of the calculated proton flux with respect to the observations. Suprathermal particles are accelerated on the magnetic field lines with negative velocity divergence ($\nabla \cdot \mathbf{u} < 0$). The strength of the acceleration is fully dependent on the jump of plasma velocity, that is, the shock strength (Sokolov et al., 2004).

10.1029/2023SW003729

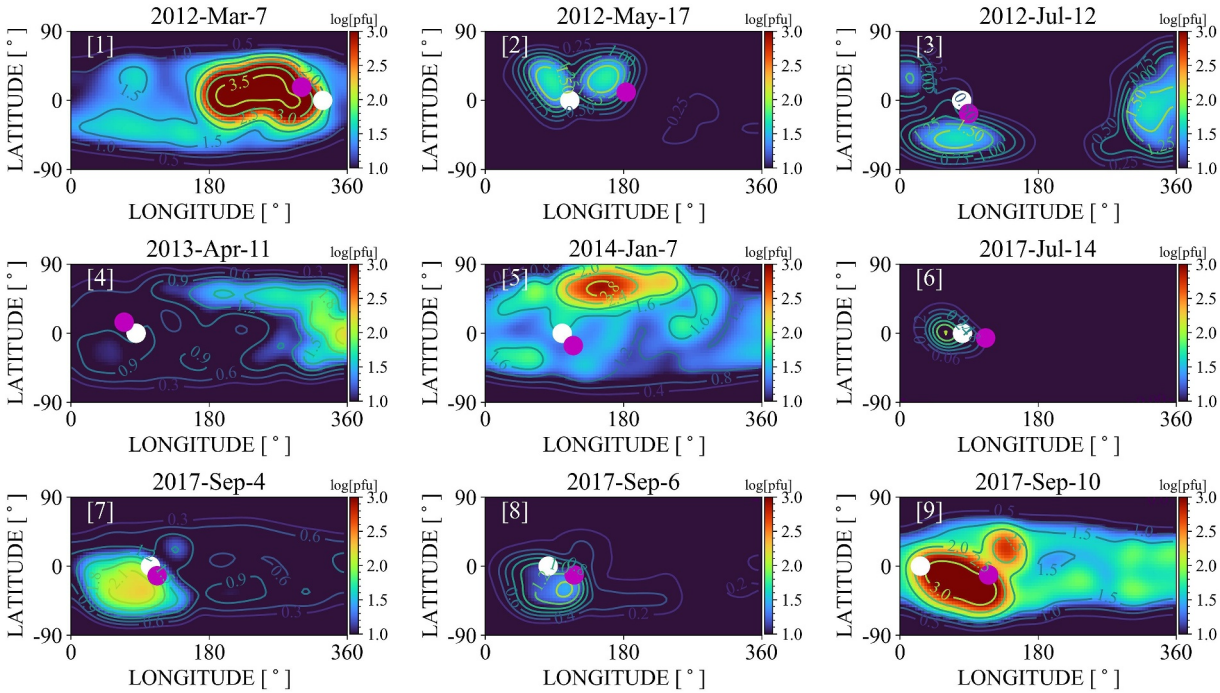

Figure 5. 2D distribution of energetic proton flux at energies greater than 10 MeV. The proton flux is plotted in the logarithm scale. The nine events are plotted in the row-wise order. The *x* and *y* axis shows the Carrington longitude and latitude on the sphere at 1 AU. The locations of Earth are marked with white solid circle, and the location of the inserted flux rope on the Sun are marked with magenta solid circle.

4.4. 2D Distribution of Proton Flux

Figure 5 shows the 2D distribution of the logarithm of the energetic proton flux 1 hr after the launch of the CME flux rope, at energies greater than 10 MeV. The *x* and *y* axis shows the Carrington longitude and latitude for a sphere at 1 AU. Earth location is marked with a white solid circle, and the location of the inserted flux rope on the Sun is marked with a magenta solid circle. The locations of the flux rope are marked in the plot to show the relative locations of Earth with respect to the CME, that is, the source of energetic particles. Since the interplanetary magnetic fields follow the Parker spiral in general (e.g., Zhao et al., 2019), the flux of energetic particles is distributed around 45°–65° eastern of the flux rope location, depending on the corona and interplanetary magnetic field configurations. In this set of runs, the injection coefficients are assumed to be uniform across the shock front (shock obliquity independent). Therefore, the 2D distribution of the energetic particles reflects the collective effect of the strength of the shock, the ambient plasma density and the temperature of the flux rope.

In the 7 March 2012 event, the parent CME erupted from the AR located at N17E15 (see Table 1), 15 degrees east of the Earth's longitude. The 2D proton flux distribution in Figure 5 shows maxima around 90 degree eastern of the Earth's location, which is consistent with the overall topology of the interplanetary magnetic fields. In the 17 May 2012 event, the parent CME erupted from the west limb, around 90 degree western of the Earth's longitude. There are two local maxima in the 2D distribution of proton flux, which may be due to the non-uniform strength of the shock driven in front of the propagating flux rope that affects the acceleration process, or the variations of the ambient plasma properties that determines the suprathermal injection. We examined the shock structure in this simulation and found the local maxima is likely due to the non-uniform shock compression ratio along the shock front.

In the 12 July 2012 event, the parent CME erupted from near central meridian as seen from Earth. Since the propagation direction of the CME leans toward the south, the proton flux in the southern hemisphere was also elevated due to the southern portion of the flux rope. In the 11 April 2013 event, the parent CME erupted from the AR located 12 degree eastern of Earth, which is consistent with the 2D distribution of proton flux shown in Figure 5. As we discussed in Section 4.2, the northern part of the CME is brighter than the southern part in the white-light image of the simulation, due to the high-density region in front of the flux rope. Such an asymmetry

Table 2
Scaling Factors of the Nine Solar Energetic Particle Events

Event	Scaling factor
7 March 2012	5
17 May 2012	0.025
12 July 2012	0.025
11 April 2013	1.25
7 January 2014	2.5
14 July 2017	0.00025
4 September 2017	0.25
6 September 2017	0.025
10 September 2017	1.25

structure was reflected in the 2D distribution plot of proton flux. The proton flux was elevated in the northern hemisphere and extended to a broader region than in the southern hemisphere, corresponding to a stronger particle source in the north.

In the 7 January 2014 event, the CME erupted from the AR located at S15W11. However, the 2D proton flux distribution shows local maxima far away from the expected region. This is due to the fine-tuning process that we performed in matching the white-light images between the observations and simulations as discussed in Section 4.2. The flux rope was inserted to an AR to the west separated by 8 degrees in longitude from the AR that was responsible for the eruption. Meanwhile, the flux rope was also rotated in order to match the simulation with the observations, which leads to the unexpected northward propagation of flux rope. In the 14 July 2017 event, the parent CME erupted from S09W33, consistent with the 2D distribution of proton flux. Note that in panel [6] of Figure 5, Earth is very close to the center of the distribution.

The 4 September 2017, 6 September 2017, and 10 September 2017 are a sequence of events that their parent CMEs erupted from the same AR located at 16, 34, and 88 degrees western of the Earth's longitude. As shown in panels [7], [8], and [9] of Figure 5, the Earth's location was on the western, close to the center, and eastern of the energetic proton source.

The 2D distribution of the energetic proton flux highly depends on the shock properties, that is, shock strength, along the connected magnetic field lines with the corresponding CME. Furthermore, the absolute particle flux is determined by the number of seed particles that are injected into the shock system. In plotting the 2D distributions shown in Figure 5, we scaled the calculated proton flux for each individual event in order to match with the >10 MeV proton flux observed by the GOES satellite, as shown below. The scaling factors are summarized in Table 2 and will be discussed in detail below. Note that for some events, the scaling factor is much larger than 1, for example, the 7 March 2012 event and 7 January 2014 event. There are many reasons that could lead to such large scaling factors. One of the reasons is the underestimation of the pre-existing seed particle sources at the event eruption, including the preceding CMEs and the flares. Another factor is the combined effect of the magnetic connectivity between the CME shock front and the earth's location with neglecting the perpendicular diffusion in the calculation. A small displacement of the earth's magnetic footpoint with respect to the shock front, together with an overestimation/underestimation of the CME shock properties will lead to a large variation of the proton flux. In this work, the perpendicular diffusion is not modeled; therefore, the proton flux contribution from cross-field diffusion, which is very important for poorly-connected events, is missing.

4.5. Time Profiles

Figure 6 compares proton flux measured by GOES with the time-dependent flux profiles obtained from the simulations. The flux profiles are calculated by extracting the >10 MeV proton flux at Earth's location from series of 2D particle distributions as shown in Figure 5. A total of 20 hr is plotted. The horizontal dashed lines represent the 10 pfu threshold used by users to determine whether the radiation caused by the energetic protons raises any concern. The four vertical dashed lines indicate the times 1, 5, 10, and 15 hr after the eruption of the CME flux rope. As we mentioned above, the absolute proton flux is multiplied by a factor of the scaling factor in order to get comparable match between observations and simulations. Therefore, in the following discussion, we focus on the rising phase and relative level of the flux profiles.

Based on the relative location of Earth with respect to the source of energetic protons, a prompt onset of protons is expected for the events when Earth is well-connected to the source of energetic protons. While the proton flux is expected to show a gradual increase if Earth's location falls outside of the particle source. As shown in the 2D distribution of energetic protons (Figure 5), in most of these events, Earth's location is on the edge of the particle distribution at 1 AU, including the 7 March 2012, 17 May 2012, 14 July 2017, 4 September 2017, 6 September 2017, and 10 September 2017 events. In the 12 July 2012, 11 April 2013, and 7 January 2014 events, the Earth location is far away from the particle distribution at 1 AU. The change of the proton flux with time, especially in

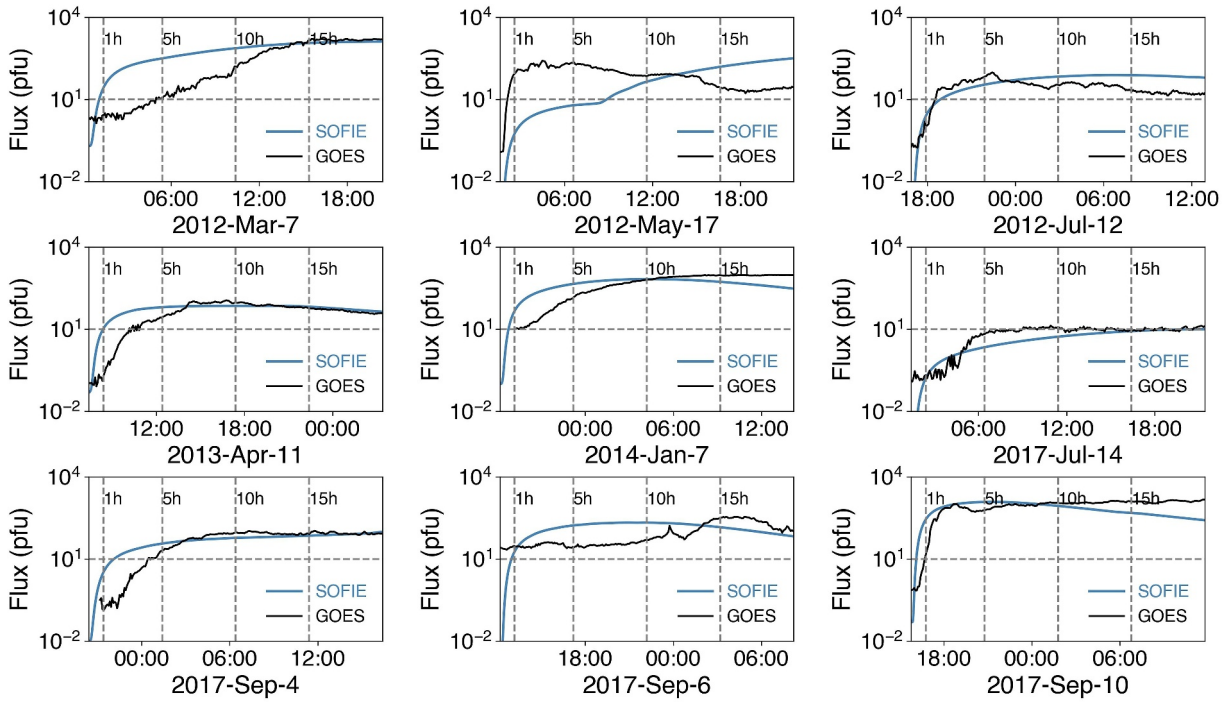

Figure 6. The comparison of proton flux at energies greater than 10 MeV between observations (black) and simulation (blue). Nine events are plotted in the row-wise order. The horizontal dashed line represents the threshold of 10 pfu and the four vertical dashed lines represent 1, 5, 10, and 15 hr after the coronal mass ejection (CME) eruption. A total time period of 20 hr after the CME eruption is shown.

the early phase, depends on the time evolution of the CME-driven shock flux rope, together with the change of magnetic connectivity between Earth and the shock CME.

The comparison between the simulations and observations shown in Figure 6 displays some discrepancies. A number of factors could contribute to these discrepancies. One of them is the background solar wind medium where the CME flux rope and energetic protons propagate. The solar wind background in this work is a steady-state solution driven by the solar magnetic fields obtained right before the flare eruption, and the 3D solar wind solution has been compared to measurements obtained from a single near-Earth point in space that might not be representative of all the medium sampled by the particles as they propagate. And the solar wind disturbances, including ICMEs, which are abundant during solar maximum, are not modeled. The second factor is that the longitudinal extent of the shock may be underestimated/overestimated. The CME flux-rope white-light simulation images have been validated with plane-of-sky images of the LASCO/C2 observation that do not include the extent of the CME in longitude. The third factor is the assumption of the same constant parallel mfp in all SEP events and the lack of cross-field diffusion processes when modeling energetic particle transport in interplanetary space. With these factors, we discuss the comparisons between simulations and observations for all the events in details below.

In the 7 March 2012 event, the proton flux calculated from the simulation shows a prompt increase, which is different from the gradual increase in the observation. This may due to the CME-driven shock is narrower in the observation than in the simulation. The scaling factor is estimated to be 5. As discussed in Section 3, there are two CME eruptions associated with this event, and the energetic particles from these two eruptions merged together after the two clear onset phases. Therefore, the scaling factor, 5 for this event, may reflect the contribution of the two eruptions. Besides, the >10 MeV proton flux was already elevated before the onset of this event from the observations. The pre-event elevated proton flux is due to a CME eruption that occurred on 4 March 2012 at 11:00:07 UT (CDAW).

In the 17 May 2012 event, the onset phase matches well between the observation and simulation. The second enhancement of proton flux at around 7 hr after the CME eruption was due to the CME evolution and the fact that Earth's magnetic connectivity changed, establishing a connection with a region with larger proton flux. Due to the

second enhancement of the proton flux, the scaling factor for this event does not reflect the difference of the overall level of proton flux between simulation and observation.

In the 12 July 2012 event, the timing of proton flux in the simulation matches very well with the observations, especially in the early phase. The mismatch of the decay of the proton flux after 10 hr may due to the assumption of the mfp in the simulation. The effect of the mfp on the decay phase of the proton flux will be discussed below.

In the 11 April 2013 event, the calculated proton flux shows a quicker onset phase than the observations. The slower onset may due to the poor magnetic connection of Earth to the CME (with an AR of N09E12). The proton flux after 6 hr between observation and simulation matches quite well and the scaling factor of 1.25 is a reasonable value.

The 7 January 2014 is a special case, as we discussed above. The 2D proton flux distribution shows the particle source is far away from the expected region, due to the fine-tuning processes of the inserted flux rope. Moreover, the >10 MeV proton flux in the observation was well-above the background due to a previous eruption that occurred at 08:00 UT on 2014 January 06.

The gradual onset phase in the 14 July 2017 event matches well between observation and simulation. The scaling factor in this event is estimated to be $2.5 \cdot 10^{-4}$. This small value could be due to the slower speed of the parent CME, 750 km s^{-1}. However, the CME speed in the 11 April 2013 event is 743 km s^{-1}, comparable to the one in the 14 July 2017 event, but the 11 April 2013 event has a scaling factor of 1.25. Another reason for the small scaling factor is that the eruption of the 14 July 2017 event was near solar minimum, when the solar activity was low, and the remnant population of prior SEP events that could act as seed particle population for the processes of particle acceleration at the shock could also be low (e.g., L. Ding et al., 2013; Gopalswamy et al., 2004; Li et al., 2012; Wijsen et al., 2023, and reference therein).

The 4 September 2017, 6 September 2017, and 10 September 2017 are a series of events that their parent CMEs erupted from the same AR. The scaling factors in these three events are 0.25, 0.025, and 1.25. The CMEs associated with the 4 September 2017 event are twin-CMEs (Li et al., 2012) as we discussed in Section 3 and shown in Figure 4. The more efficient acceleration in the twin-CME system (L. Ding et al., 2013; Li et al., 2012; Zhao & Li, 2014) could be one of the potential reasons why the scaling factor in this event is much larger than the 14 July 2017 event, although this event occurred under solar minimum conditions. The 6 September 2017 event occurred in the decay phase of the 4 September 2017 event. Therefore, the onset phase between the observation and simulation does not compare well. The onset phase in the 10 September 2017 event calculated from the simulation is faster than the observation. This may due to the overall extension of the CME flux rope and the magnetic connectivity at the beginning of the event. Similar to the 12 July 2012 event, the decay phase in the simulation is faster than the simulation, indicating a faster deceleration of the CME in the simulations or a larger mfp assumption.

The determination of the scaling factor in each individual event is affected by the properties of the shocks driven by the eruption of the CME flux rope, including the spatial extension of the shock surfaces and the strengths of the shocks. Hence, the value of the scaling factor does not necessarily imply that there are more or less suprathermal protons, in the energy of 10 keV, that are accelerated in the DSA processes. An estimation of a larger CME flux rope or a stronger CME-driven shock will lead to a smaller scaling factor and vice versa. Besides, the magnetic connectivity between Earth's location and the CME shock front also affects the scaling factor. If the Earth's location is close to the edge of the particle source, a small change of the size of the CME flux rope or a little error in the magnetic connectivity calculation will result in a larger or smaller scaling factor. In Figures 2–4, the comparison between simulation and observation is only performed for the SOHO/C2 observations, which include a large projection effect. In the future work, a multi-spacecraft validation of the white-light CME image will be included. Moreover, together with C2 observation, C3 observation will also be used to monitor the acceleration or deceleration of the CME flux rope in the solar corona. The onset phase contains competing processes between the continuous acceleration of protons and the diffusion process. Therefore, a significant deceleration of the CME flux rope propagation in the very early phase would reduce the acceleration efficiency of energetic protons, especially in the higher energy end.

4.6. 11 April 2013 Event

Since SOFIE calculates the distribution function of energetic protons along the extracted magnetic field lines, in this section, we will show both the differential and integral proton fluxes, using the 11 April 2013 event as an

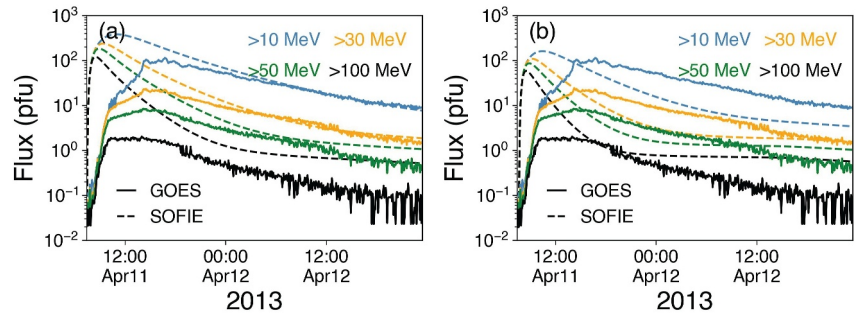

Figure 7. Comparison between simulations and observations for the 11 April 2013 event. Time profiles of two selected magnetic field lines are shown. The fluxes shown in panel (a) are calculated on the magnetic field line that is 50° east of earth's location, and the fluxes shown in panel (b) are calculated on the magnetic field line that is closest to the earth. Time profiles of protons in the energies of >10, >30, >50, and >100 MeV are plotted in blue, yellow, green, and black colors. Observations are plotted in solid and simulations are plotted in dashed lines.

example. In Figure 7, proton fluxes in the energies of >10, >30, >50, and >100 MeV are plotted in blue, yellow, green, and black colors respectively. These energy channels are chosen because they are relevant to operational forecasts. Calculated proton fluxes on two magnetic field lines are plotted in dashed curves, and observed proton fluxes are plotted in solid curves. The fluxes shown in panel (a) are calculated on the magnetic field line 50° east of the earth's location (field line #1) and the fluxes shown in panels (b) are calculated on the magnetic field line that is closest to the earth location (field line #2). The field line #1 is chosen because it was connected to the nose of the shock in the beginning of the event, and the field line #2 is chosen because it was connected to the earth's vicinity.

The proton fluxes calculated on field line #2 are smaller than those calculated on field line #1 because the field line #1 is connected to the nose of the shock and the field line #2 is connected to the west flank of the shock at the beginning of the event. The particle acceleration process is more efficient, with a higher compression ratio, in the shock nose region than in the flank region, with a lower compression ratio. In panel (a), when the >10 and >30 MeV proton fluxes match between simulations and observations in the decay phase, the >50 and >100 MeV proton flux are over estimated in the simulations.

In Figure 8, we plot the calculated differential intensities in 6 energy channels and compare them with the observation made by SOHO/Energetic and Relativistic Nuclei and Electron (ERNE) instrument (Torsti et al., 1995). Simulation results are plotted in dashed curves and the observations are plotted in solid circles. The 6 energy channels are chosen between 1 and 20 MeV. The same scaling factor as used in Figure 7 is applied to all simulation results. The onset times in simulations match well with the observations in all 6 energy channels, with a clear velocity dispersion. For the two high energy channels (10.0–13.0 and 16.0–20.0 MeV), the onset phases of the simulations are faster in the simulations than in the observations. For the two low energy channels (1.6–2.0 and 2.5–3.2 MeV), the onset phases of the simulations are slower in the simulations than in the observations. The onset phases between simulations and observations are comparable for the two intermediate energy channels (4.0–5.0 and 6.4–8.0 MeV). The decay phase of all energy channels match between simulations and observations.

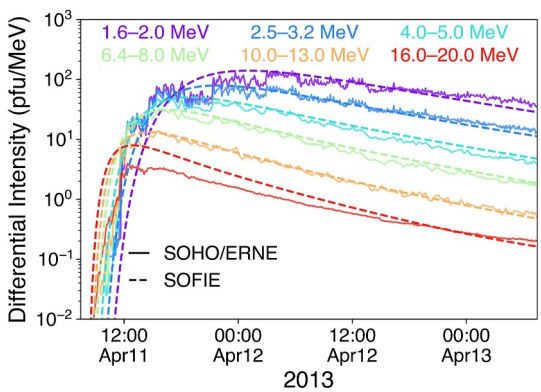

Figure 8. Comparison of the calculated differential intensity with Solar and Heliospheric Observatory/Energetic and Relativistic Nuclei and Electron (SOHO/ERNE) observations for the 11 April 2013 event. Time intensity profiles of the SOHO/ERNE observations are plotted in solid curves and the calculated intensities are plotted in dashed curves. Six energy channels that range from 1 to 20 MeV are shown. The same scaling factor is applied as in Figure 7.

5. Discussion

In this paper, we describe the physics-based SEP model, SOFIE, and its application in modeling nine historical SEP events. The simulations of the SEP events start from calculating the background solar wind using the AWSoM-R model, in which the solution of the solar wind plasma is driven by the measurement of the Sun's magnetic field. The acceleration of energetic protons in SOFIE is solved in the CME-driven shock generated by the eruption of a force-imbalanced flux rope inserted in the corresponding AR on

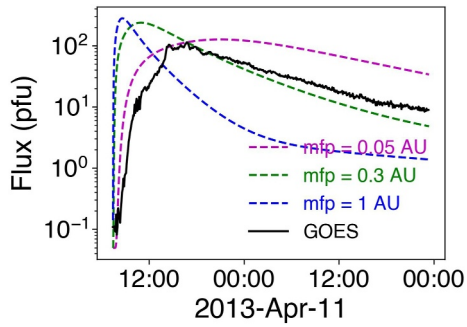

Figure 9. The effect of far-upstream mean free paths (mfp) on the calculated proton flux profiles in the 11 April 2013 event. The Geostationary Operational Environmental Satellite observation is plotted in black. The calculated proton flux profiles with different mfp are plotted in magenta (mfp = 0.05 AU), green (mfp = 0.3 AU), and blue (mfp = 1 AU).

the Sun using the EEGGL model. The acceleration and transport of energetic protons are modeled using the M-FLAMPA model, in which the Parker diffusion equations are solved along individual time-evolving magnetic field lines.

In this work, we perform a systematic test of using SOFIE model to forecast proton flux in the energies of >10 MeV in SEP events. The steady-state background solar wind macroscopic properties (radial solar wind speed, number density, temperature, total magnetic field strength) calculated from the AWSoM-R are compared and validated against in-situ measurements. The white-light coronagraph images of the erupted flux rope generated by the CME generator, EEGGL, are compared and evaluated with SOHO/LASCO/C2 observations. This is only a single-observer comparison, therefore, the longitudinal extent of the flux rope has not been compared to observations. The proton flux at energies greater than 10 MeV calculated by M-FLAMPA is compared with GOES observation for the first 20 hr. In order to obtain a comparable flux level with observations, different The differences between the proton flux calculated in SOFIE and the observation are represented by the scaling factors. The potential factors that may affect the scaling factors include the multiple CME eruptions in one SEP event, the elevated suprathermal particles from previous eruptions, and solar activity level (see L. Ding et al., 2013; Gopalswamy et al., 2004; Li et al., 2012; Wijsen et al., 2023, and reference therein).

In the current set of runs, the upstream mfps are assumed to be the same for all the events for simplicity. This assumption may lead to a faster or slower decay profile in the simulation as shown in Figure 9. In Figure 9, we plot the proton fluxes in the energies of >10 MeV with different mfps. Here, the magenta, green, and blue dashed curves show the flux profiles with far-upstream mfps of 0.05, 0.3, and 1 AU. Not only the absolute flux level, the onset phase and the decay phases depend on the value of mfps. Employing the turbulence strength calculated from the MHD simulation is one of the future steps to improve the SOFIE model. This also emphasizes the importance and necessity to transport energetic particles in the solar wind solution calculated from an MHD simulation. The transport of energetic particles in interplanetary space involves many different physical processes, including adiabatic cooling, magnetic focusing, as well as parallel and perpendicular diffusion. All these processes depend on the properties of ambient solar wind background. The magnetic field turbulence affects the timing of the first arriving particles, the timing when the particle flux crosses a pre-set threshold (Qin et al., 2006; Wang & Qin, 2015), and the time-dependent and event-integrated energy spectral index (Zhao et al., 2016, 2017).

Besides the steady-state background solar wind, CMEs and ICMEs, which are the main accelerators of energetic particles travel through the ambient solar wind medium, interact with its surrounding plasma and magnetic field, causing significant distortions and disruptions of the solar wind plasma (Manchester, Gombosi, Roussev, Ridley, et al., 2004; Manchester, Gombosi, Roussev, Zeeuw, et al., 2004; Manchester et al., 2005, 2008, 2012). These distortions affect the acceleration and transport of energetic particles. There are also SEP events that are associated with more than one CME eruption, for example, the 7 March 2012 and 4 September 2017 events. The underlying acceleration of energetic particles is likely to be enhanced according to the twin-CME scenario (L. Ding et al., 2013; Li et al., 2012; Zhao & Li, 2014). In this work, when modeling the nine historical SEP events, each event is only associated with one CME eruption and the simulation of the background medium does not include prior CMEs that could affect the transport of SEPs. In future work, we will examine the performance of SOFIE in modeling more than one CME eruption.

6. SOFIE as an SEP Forecast Tool

We have run nine historical SEP events to show the capability of SOFIE in simulating the >10 MeV proton flux. In the simulations, the most time and resource-consuming part is simulating the propagation of CME fluxrope in the solar corona domain (1.05–20 R_s). In the current setup, the SOFIE model runs at the same speed as real-time with 2,000 cpu cores using NASA Pleiades supercomputer. SOFIE will run faster than real-time when more cpu cores are used. When the CME flux rope leaves the solar corona domain, that is, several hours after the CME eruption, SOFIE runs much faster than real-time, thus empowering the capability of using SOFIE to predict the properties of SEP events.

When making a prediction, the background solar wind solution will be updated every hour using the hourly updated GONG magnetic field measurement of the sun. Then SOFIE will run in both post-eruption and pre-eruption mode. In the post-eruption mode, the CME flux rope will be launched from the parent AR when the CME is observed by SOHO/LASCO or future solar coronagraph imager. The leading time of the prediction depends on the delay of the GONG magnetic field measurement and the CME observations. According to the current GONG website (https://gong.nso.edu/data/magmap/QR/bqs/) and the description on the LASCO website (https://lasco-www.nrl.navy.mil/index.php?p=content/retrieve/levels), the GONG magnetic field measurement has a delay of less than 1 hour and the observation will be either available in near-real-time or delayed by a few hours. Therefore, SOFIE could predict the proton flux up to a few hours of delay at the beginning of the event and faster than real time in the later phase of the event when CME propagates out of the corona domain. SOFIE will also run in pre-eruption mode when coupled with the CME prediction models. In the pre-eruption mode, flux rope will be launched from the AR when a CME is predicted from an AR (Zhao, 2023a). The leading time in the pre-eruption mode can be up to 24 hr. In the pre-eruption mode, we will use the GONG magnetogram that is immediately available when the predicted CME is launched to drive the background solar wind.

When SOFIE will be used as a prediction tool, the free parameters will be set as default or calculated based on empirical formulae. The free parameters of SOFIE include the Poynting flux and the correlation length of the Alfvén wave dissipation in the background solar wind module (Section 4.1), the upstream mfp and the injection coefficient in the M-FLAMPA module. In the work of Z. Huang et al. (2023, 2024), the solar cycle dependence of the Poynting flux and correlation length has been studied. When SOFIE will be used as the prediction tool, these two parameters will be determined based on the empirical formulas suggested in Z. Huang et al. (2023, 2024). In M-FLAMPA, the upstream mfp is set to be 0.3 AU and the injection coefficient is set to be 1 as default. Table 2 shows that, in five out of nine events, the predicted proton fluxes are within an order of magnitude with the observations, satisfying the operational necessities (Vourlidas et al., 2021).

Data Availability Statement

The in situ solar wind plasma properties used in this work are available in the Space Physics Data Facility https://spdf.gsfc.nasa.gov/. The white-light image data is available in the SOHO/LASCO website https://lasco-www.nrl.navy.mil/index.php?p=content/retrieve/products. The GOES data are available at https://www.ngdc.noaa.gov/stp/satellite/goes/index.html. All simulation data including the 3D steady-state solution of the solar wind plasma, the 2D white-light image data, the 2D distribution of protons, and the time-dependent flux profiles are publicly available at the Deep Blue Data Repository maintained by the University of Michigan (Zhao, 2023b).

Acknowledgments

This work was supported in part by NASA LWS Strategic Capabilities (SCEPTER) project at the University of Michigan under NASA Grant 80NSSC22K0892, NASA Space Weather CoE CLEAR Grant 80NSSC23M0191, NASA LWS Grant 80NSSC21K0417, NASA R2O2R Grant 80NSSC22K0269, NASA HSR Grant 80NSSC23K0091, NSF ANSWERS Grant GEO-2149771. D.L. acknowledges support also from NASA Living With a Star program NNH19ZDA001N-LWS, and the Heliophysics Innovation Fund program of the Goddard Space Flight Center. We thank the ACE SWEPAM instrument team and the ACE Science Center for providing the ACE data. We thank the SOHO project, an international cooperation between ESA and NASA. We thank the GOES team. This work utilizes data from the National Solar Observatory Integrated Synoptic Program, which is operated by the Association of Universities for Research in Astronomy, under a cooperative agreement with the National Science Foundation and with additional financial support from the National Oceanic and Atmospheric Administration, the National Aeronautics and Space Administration, and the United States Air Force. The GONG network of instruments is hosted by the Big Bear Solar Observatory, High Altitude Observatory, Learmonth Solar Observatory, Udaipur Solar Observatory, Instituto de Astrofísica de Canarias, and Cerro Tololo Interamerican Observatory. Resources supporting this work were provided, in part, by the NASA High-End Computing (HEC) Program through the NASA Advanced Supercomputing (NAS) Division at Ames Research Center. The authors acknowledge the Texas Advanced Computing Center (TACC) at The University of Texas at Austin for providing HPC resources that have contributed to the research results reported within this paper. http://www.tacc.utexas.edu.

References

Afanasiev, A., Vainio, R., Trotta, D., Nyberg, S., Talebpour Sheshvan, N., Hietala, H., & Dresing, N. (2023). Self-consistent modeling of the energetic storm particle event of November 10, 2012. *Astronomy & Astrophysics*, *679*, A111. https://doi.org/10.1051/0004-6361/202346220

Alberti, T., Laurenza, M., Cliver, E. W., Storini, M., Consolini, G., & Lepreti, F. (2017). Solar activity from 2006 to 2014 and short-term forecasts of solar proton events using the ESPERTA model. *The Astrophysical Journal*, *838*(1), 59. https://doi.org/10.3847/1538-4357/aa5cb8

Alho, M., Wedlund, C. S., Nilsson, H., Kallio, E., Jarvinen, R., & Pulkkinen, T. (2019). Hybrid modeling of cometary plasma environments. *Astronomy & Astrophysics*, *630*, A45. https://doi.org/10.1051/0004-6361/201834863

Anastasiadis, A., Papaioannou, A., Sandberg, I., Georgoulis, M., Tziotziou, K., Kouloumvakos, A., & Jiggens, P. (2017). Predicting flares and solar energetic particle events: The FORSPEF tool. *Solar Physics*, *292*(9), 134. https://doi.org/10.1007/s11207-017-1163-7

Aran, A., Pacheco, D., Agueda, N., & Sanahuja, B. (2017). Updating SOLPENCO2 and new analysis on downstream FLuence (SOL2UP) project. In *Final report, ESA/ESTEC contract 4000114116/15/NL/HK* (pp. 1–90).

Axford, W. I., Leer, E., & Skadron, G. (1977). The acceleration of cosmic rays by shock waves. In *International cosmic ray conference* (Vol. 11, p. 132)

Bain, H. M., Steenburgh, R. A., Onsager, T. G., & Stitely, E. M. (2021). A summary of national oceanic and atmospheric administration space weather prediction center proton event forecast performance and skill. *Space Weather*, *19*(7), e02670. https://doi.org/10.1029/2020sw002670

Balabin, Y. V., Germanenko, A. V., Vashenyuk, E. V., & Gvozdevsky, B. B. (2013). The first GLE of new 24th solar cycle. In *International cosmic ray conference* (Vol. 33, p. 1467)

Balch, C. C. (2008). Updated verification of the space weather prediction center's solar energetic particle prediction model. *Space Weather*, *6*(1), 1–13. https://doi.org/10.1029/2007sw000337

Bell, A. R. (1978a). The acceleration of cosmic rays in shock fronts. I. *MNRAS*, *182*(2), 147–156. https://doi.org/10.1093/mnras/182.2.147

Bell, A. R. (1978b). The acceleration of cosmic rays in shock fronts. II. *MNRAS*, *182*(3), 443–455. https://doi.org/10.1093/mnras/182.3.443

Belov, A. (2009). Properties of solar X-ray flares and proton event forecasting. *Advances in Space Research*, *43*(4), 467–473. https://doi.org/10.1016/j.asr.2008.08.011

Blandford, R. D., & Ostriker, J. P. (1978). Particle acceleration by astrophysical shocks. *The Astrophysical Journal Letters*, *221*, L29–L32. https://doi.org/10.1086/182658

Bloomfield, D. S., Higgins, P. A., McAteer, R. T., & Gallagher, P. T. (2012). Toward reliable benchmarking of solar flare forecasting methods. *The Astrophysical Journal Letters*, *747*(2), L41. https://doi.org/10.1088/2041-8205/747/2/l41

Bobra, M. G., & Couvidat, S. (2015). Solar flare prediction using SDO/HMI vector magnetic field data with a machine-learning algorithm. *The Astrophysical Journal*, *798*(2), 135. https://doi.org/10.1088/0004-637x/798/2/135

Bobra, M. G., & Ilonidis, S. (2016). Predicting coronal mass ejections using machine learning methods. *The Astrophysical Journal*, *821*(2), 1–7. https://doi.org/10.3847/0004-637x/821/2/127

Borovikov, D., Sokolov, I. V., Manchester, W. B., Jin, M., & Gombosi, T. I. (2017). Eruptive event generator based on the Gibson-Low magnetic configuration. *Journal of Geophysical Research*, *122*(8), 7979–7984. https://doi.org/10.1002/2017ja024304

Borovikov, D., Sokolov, I. V., Roussev, I. I., Taktakishvili, A., & Gombosi, T. I. (2018). Toward a quantitative model for simulation and forecast of solar energetic particle production during gradual events. I. Magnetohydrodynamic background coupled to the SEP model. *The Astrophysical Journal*, *864*(1), 88. https://doi.org/10.3847/1538-4357/aad68d

Boubrahimi, S. F., Aydin, B., Martens, P., & Angryk, R. (2017). On the prediction of >100 MeV solar energetic particle events using GOES satellite data. In *IEEE international conference on Big data (BIGDATA)* (pp. 2533–2542).

Boucheron, L. E., Al-Ghraibah, A., & McAteer, R. T. (2015). Prediction of solar flare size and time-to-flare using support vector machine regression. *The Astrophysical Journal*, *812*(1), 51. https://doi.org/10.1088/0004-637x/812/1/51

Brueckner, G., Howard, R. A., Koomen, M. J., Korendyke, C. M., Michels, D. J., Moses, J. D., et al. (1995). The large angle spectroscopic coronagraph (LASCO). *Solar Physics*, *162*, 357–402. https://doi.org/10.1007/978-94-009-0191-9_10

Bruno, A., Christian, E. R., de Nolfo, G. A., Richardson, I. G., & Ryan, J. M. (2019). Spectral analysis of the September 2017 solar energetic particle events. *Space Weather*, *17*(3), 419–437. https://doi.org/10.1029/2018SW002085

Cane, H. V., & Richardson, I. G. (2003). Interplanetary coronal mass ejections in the near-earth solar wind during 1996–2002. *Journal of Geophysical Research*, *108*(A4), 1156. https://doi.org/10.1029/2002JA009817

Chertok, I. M., Belov, A. V., & Abunin, A. A. (2018). Solar eruptions, Forbush decreases, and geomagnetic disturbances from outstanding active region 12673. *Space Weather*, *16*(10), 1549–1560. https://doi.org/10.1029/2018SW001899

Cohen, C. M. S., Mason, G. M., Mewaldt, R. A., & Wiedenbeck, M. E. (2014). The longitudinal dependence of heavy-ion composition in the 2013 April 11 solar energetic particle event. *The Astrophysical Journal*, *793*(1), 35. https://doi.org/10.1088/0004-637X/793/1/35

Colak, T., & Qahwaji, R. (2009). Automated solar activity prediction: A hybrid computer platform using machine learning and solar imaging for automated prediction of solar flares. *Space Weather*, *7*(6), 1–12. https://doi.org/10.1029/2008sw000401

Ding, L., Jiang, Y., Zhao, L., & Li, G. (2013). The "Twin-CME" scenario and large solar energetic particle events in solar cycle 23. *The Astrophysical Journal*, *763*(1), 30. https://doi.org/10.1088/0004-637x/763/1/30

Ding, Z., Li, G., Hu, J.-X., & Fu, S. (2020). Modeling the 2017 September 10 solar energetic particle event using the iPATH model. *Research in Astronomy and Astrophysics*, *20*(9), 145. https://doi.org/10.1088/1674-4527/20/9/145

Drury, L. O. (1983). An introduction to the theory of diffusive shock acceleration of energetic particles in tenuous plasmas. *Reports on Progress in Physics*, *46*(8), 973–1027. https://doi.org/10.1088/0034-4885/46/8/002

Engell, A. J., Falconer, D. A., Schuh, M., Loomis, J., & Bissett, D. (2017). SPRINTS: A framework for solar-driven event forecasting and research. *Space Weather*, *15*(10), 1321–1346. https://doi.org/10.1002/2017sw001660

Falconer, D. A., Moore, R. L., Barghouty, A. F., & Khazanov, I. (2014). MAG4 versus alternative techniques for forecasting active region flare productivity. *Space Weather*, *12*(5), 306–317. https://doi.org/10.1002/2013sw001024

Fisk, L. A., & Gloeckler, G. (2007). Thermodynamic constraints on stochastic acceleration in compressional turbulence. *Proceedings of the National Academy of Sciences*, *104*(14), 5749–5754. https://doi.org/10.1073/pnas.0700881104

Fulara, A., Chandra, R., Chen, P. F., Zhelyazkov, I., Srivastava, A. K., & Uddin, W. (2019). Kinematics and energetics of the EUV waves on 11 April 2013. *Solar Physics*, *294*(5), 56. https://doi.org/10.1007/s11207-019-1445-3

Garcia, H. A. (2004). Forecasting methods for occurrence and magnitude of proton storms with solar soft X rays. *Space Weather*, *2*(6), S02002. https://doi.org/10.1029/2003sw000001

García-Rigo, A., Núñez, M., Qahwaji, R., Ashamari, O., Jiggens, P., Pérez, G., et al. (2016). Prediction and warning system of SEP events and solar flares for risk estimation in space launch operations. *Journal of Space Weather and Space Climate*, *6*, A28. https://doi.org/10.1051/swsc/2016021

Georgoulis, M. K. (2008). Magnetic complexity in eruptive solar active regions and associated eruption parameters. *Geophysical Research Letters*, *35*(6), 5–9. https://doi.org/10.1029/2007gl032040

Giacalone, J. (2003). The physics of particle acceleration by collisionless shocks. *Planetary and Space Science*, *51*(11), 659–664. https://doi.org/10.1016/S0032-0633(03)00101-6

Giacalone, J. (2005a). The efficient acceleration of thermal protons by perpendicular shocks. *The Astrophysical Journal*, *628*(1), L37–L40. https://doi.org/10.1086/432510

Giacalone, J. (2005b). Particle acceleration at shocks moving through an irregular magnetic field. *The Astrophysical Journal*, *624*(2), 765–772. https://doi.org/10.1086/429265

Giacalone, J., & Kóta, J. (2006). Acceleration of solar-energetic particles by shocks. *Space Science Reviews*, *124*(1), 277–288. https://doi.org/10.1007/s11214-006-9110-1

Gibson, S. E., & Low, B. C. (1998). A time-dependent three-dimensional magnetohydrodynamic model of the coronal mass ejection. *The Astrophysical Journal*, *493*(1), 460–473. https://doi.org/10.1086/305107

Gil, A., Modzelewska, R., Moskwa, S., Siluszyk, A., Siluszyk, M., Wawrzynczak, A., et al. (2020). The solar event of 14–15 July 2012 and its geoeffectiveness. *Solar Physics*, *295*(10), 135. https://doi.org/10.1007/s11207-020-01703-2

Gombosi, T. I., Chen, Y., Glocer, A., Huang, Z., Jia, X., Liemohn, M. W., et al. (2021). What sustained multi-disciplinary research can achieve: The space weather modeling framework. *Journal of Space Weather and Space Climate*, *11*, 42. https://doi.org/10.1051/swsc/2021020

Gombosi, T. I., van der Holst, B., Manchester, W. B., & Sokolov, I. V. (2018). Extended MHD modeling of the steady solar corona and the solar wind. *LRSP*, *15*(1), 4.

Gopalswamy, N., Yashiro, S., Krucker, S., Stenborg, G., & Howard, R. A. (2004). Intensity variation of large solar energetic particle events associated with coronal mass ejections. *Journal of Geophysical Research*, *109*(A12), 105. https://doi.org/10.1029/2004ja010602

Gressl, C., Veronig, A. M., Temmer, M., Odstrčil, D., Linker, J. A., Mikić, Z., & Riley, P. (2014). Comparative study of MHD modeling of the background solar wind. *Solar Physics*, *289*(5), 1783–1801. https://doi.org/10.1007/s11207-013-0421-6

Guo, F., Giacalone, J., & Zhao, L. (2021). Shock propagation and associated particle acceleration in the presence of ambient solar-wind turbulence. *Frontiers in Astronomy and Space Sciences*, *8*, 644354. https://doi.org/10.3389/fspas.2021.644354

Hu, J., Li, G., Ao, X., Zank, G. P., & Verkhoglyadova, O. (2017). Modeling particle acceleration and transport at a 2-D CME-driven shock. *Journal of Geophysical Research Space Physics*, *122*(11), 10938–10963. https://doi.org/10.1002/2017JA024077

Huang, X., Wang, H., Xu, L., Liu, J., Li, R., & Dai, X. (2018). Deep learning based solar flare forecasting model. I. Results for line-of-sight magnetograms. *The Astrophysical Journal*, *856*(1), 7. https://doi.org/10.3847/1538-4357/aaae00

Huang, X., Wang, H. N., & Li, L. P. (2012). Ensemble prediction model of solar proton events associated with solar flares and coronal mass ejections. *Research in Astronomy and Astrophysics*, *12*(3), 313–321. https://doi.org/10.1088/1674-4527/12/3/007

Huang, Z., Tóth, G., Sachdeva, N., & van der Holst, B. (2024). Solar wind driven from GONG magnetograms in the last solar cycle. *The Astrophysical Journal*, *965*(1), 1. https://doi.org/10.3847/1538-4357/ad32ca

Huang, Z., Tóth, G., Sachdeva, N., Zhao, L., van der Holst, B., Sokolov, I., et al. (2023). Modeling the solar wind during different phases of the last solar cycle. *The Astrophysical Journal Letters*, *946*(2), L47. https://doi.org/10.3847/2041-8213/acc5ef

Inceoglu, F., Jeppesen, J. H., Kongstad, P., Marcano, N. J. H., Jacobsen, R. H., & Karoff, C. (2018). Using machine learning methods to forecast if solar flares will Be associated with CMEs and SEPs. *The Astrophysical Journal*, *861*(2), 128. https://doi.org/10.3847/1538-4357/aac81e

James, A. W., Green, L. M., van Driel-Gesztelyi, L., & Valori, G. (2020). A new trigger mechanism for coronal mass ejections. The role of confined flares and photospheric motions in the formation of hot flux ropes. *Astronomy & Astrophysics*, *644*, A137. https://doi.org/10.1051/0004-6361/202038781

Jin, M., Manchester, W. B., van der Holst, B., Sokolov, I., Tóth, G., Vourlidas, A., et al. (2017a). Chromosphere to 1 au simulation of the 2011 March 7th event: A comprehensive study of coronal mass ejection propagation. *The Astrophysical Journal*, *834*(2), 172. https://doi.org/10.3847/1538-4357/834/2/172

Jin, M., Manchester, W. B., van der Holst, B., Sokolov, I., Tóth, G., Mullinix, R. E., et al. (2017b). Data-constrained coronal mass ejections in a global magnetohydrodynamics model. *The Astrophysical Journal*, *834*(2), 173. https://doi.org/10.3847/1538-4357/834/2/173

Jin, M., Nitta, N. V., & Cohen, C. M. S. (2022). Assessing the influence of input magnetic maps on global modeling of the solar wind and CME-driven shock in the 2013 April 11 event. *Space Weather*, *20*(3), e2021SW002894. https://doi.org/10.1029/2021SW002894

Jin, M., Schrijver, C. J., Cheung, M. C. M., DeRosa, M. L., Nitta, N. V., & Title, A. M. (2016). A numerical study of long-range magnetic impacts during coronal mass ejections. *The Astrophysical Journal*, *820*(1), 16. https://doi.org/10.3847/0004-637x/820/1/16

Jing, J., Inoue, S., Lee, J., Li, Q., Nita, G. M., Xu, Y., et al. (2021). Understanding the initiation of the M2.4 flare on 2017 July 14. *The Astrophysical Journal*, *922*(2), 108. https://doi.org/10.3847/1538-4357/ac26c7

Jivani, A., Sachdeva, N., Huang, Z., Chen, Y., van der Holst, B., Manchester, W., et al. (2023). Global sensitivity analysis and uncertainty quantification for background solar wind using the Alfvén wave solar atmosphere model. *Space Weather*, *21*(1), e2022SW003262. https://doi.org/10.1029/2022SW003262

Jokipii, J. R. (1966). Cosmic-ray propagation I. charged particles in a random magnetic field. *The Astrophysical Journal*, *146*, 480. https://doi.org/10.1086/148912

Joshi, B., Kushwaha, U., Veronig, A. M., Dhara, S. K., Shanmugaraju, A., & Moon, Y.-J. (2017). Formation and eruption of a flux rope from the sigmoid active region NOAA 11719 and associated M6.5 flare: A multi-wavelength study. *The Astrophysical Journal*, *834*(1), 42. https://doi.org/10.3847/1538-4357/834/1/42

Kasapis, S., Zhao, L., Chen, Y., Wang, X., Bobra, M., & Gombosi, T. I. I. (2022). Interpretable machine learning to forecast SEP events for Solar Cycle 23. *Space Weather*, *20*(2), e02842. https://doi.org/10.1029/2021SW002842

Kataoka, R., Ebisuzaki, T., Kusano, K., Shiota, D., Inoue, S., Yamamoto, T. T., & Tokumaru, M. (2009). Three-dimensional MHD modeling of the solar wind structures associated with 13 December 2006 coronal mass ejection. *Journal of Geophysical Research*, *114*(A10), 10102. https://doi.org/10.1029/2009JA014167

Kecskeméty, K., Daibog, E. I., Logachev, Y. I., & Kóta, J. (2009). The decay phase of solar energetic particle events. *Journal of Geophysical Research*, *114*(A6), 383. https://doi.org/10.1029/2008JA013730

Kouloumvakos, A., Patsourakos, S., Nindos, A., Vourlidas, A., Anastasiadis, A., Hillaris, A., & Sandberg, I. (2016). Multi-viewpoint observations of a widely distributed solar energetic particle event: The role of EUV waves and white-light shock signatures. *The Astrophysical Journal*, *821*(1), 31. https://doi.org/10.3847/0004-637X/821/1/31

Kozarev, K. A., Davey, A., Kendrick, A., Hammer, M., & Keith, C. (2017). The coronal analysis of SHocks and waves (CASHeW) framework. *JSWSC*, *7*, A32. https://doi.org/10.1051/swsc/2017028

Kozarev, K. A., Nedal, M., Miteva, R., Dechev, M., & Zucca, P. (2022). A multi-event study of early-stage SEP acceleration by CME-driven shocks—Sun to 1 AU. *Frontiers in Astronomy and Space Sciences*, *9*, 801429. https://doi.org/10.3389/fspas.2022.801429

Krymsky, G. F. (1977). A regular mechanism for the acceleration of charged particles on the front of a shock wave. *Soviet Physics-Doklady*, *234*, 1306.

Kühl, P., Banjac, S., Dresing, N., Goméz-Herrero, R., Heber, B., Klassen, A., & Terasa, C. (2015). Proton intensity spectra during the solar energetic particle events of May 17, 2012 and January 6, 2014. *Astronomy & Astrophysics*, *576*, A120. https://doi.org/10.1051/0004-6361/201424874

Lario, D., Ho, G. C., Roelof, E. C., Anderson, B. J., & Korth, H. (2013). Intense solar near-relativistic electron events at 0.3 AU. *Journal of Geophysical Research Space Physics*, *118*(1), 63–73. https://doi.org/10.1002/jgra.50106

Lario, D., Raouafi, N. E., Kwon, R.-Y., Zhang, J., Gómez-Herrero, R., Dresing, N., & Riley, P. (2014). The solar energetic particle event on 2013 April 11: An investigation of its solar origin and longitudinal spread. *The Astrophysical Journal*, *797*(1), 8. https://doi.org/10.1088/0004-637X/797/1/8

Laurenza, M., Cliver, E. W., Hewitt, J., Storini, M., Ling, A. G., Balch, C. C., & Kaiser, M. L. (2009). A technique for short-term warning of solar energetic particle events based on flare location, flare size, and evidence of particle escape. *Space Weather*, *7*(4), 1–18. https://doi.org/10.1029/2007sw000379

Li, C., Firoz, K., Sun, L., & Miroshnichenko, L. (2013). Electron and proton acceleration during the first ground level enhancement event of solar cycle 24. *The Astrophysical Journal*, *770*(1), 34. https://doi.org/10.1088/0004-637X/770/1/34

Li, G., Jin, M., Ding, Z., Bruno, A., de Nolfo, G., Randol, B., et al. (2021). Modeling the 2012 May 17 solar energetic particle event using the AWSoM and iPATH models. *The Astrophysical Journal*, *919*(2), 146. https://doi.org/10.3847/1538-4357/ac0db9

Li, G., Moore, R., Mewaldt, R. A., Zhao, L., & Labrador, A. W. (2012). A twin-CME scenario for ground level enhancement events. *Space Science Reviews*, *171*(1–4), 141–160. https://doi.org/10.1007/s11214-011-9823-7

Linker, J. A., Caplan, R. M., Schwadron, N., Gorby, M., Downs, C., Torok, T., et al. (2019). Coupled MHD-focused transport simulations for modeling solar particle events. *Journal of Physics: Conference Series*, *1225*(1), 012007. https://doi.org/10.1088/1742-6596/1225/1/012007

Lugaz, N., Iv, W. B. M., Roussev, I. I., Tóth, G., & Gombosi, T. I. (2007). Numerical investigation of the homologous coronal mass ejection events from active region 9236 (Vol. *659*).

Lugaz, N., Manchester, W. B., & Gombosi, T. I. (2005). Numerial simulation of the interaction of two coronal mass ejections from Sun to Earth. *The Astrophysical Journal*, *634*, 651–662.

Luhmann, J., Ledvina, S., Krauss-Varban, D., Odstrcil, D., & Riley, P. (2007). A heliospheric simulation-based approach to SEP source and transport modeling. *Advances in Space Research*, *40*(3), 295–303. https://doi.org/10.1016/j.asr.2007.03.089

Manchester, W. B., Gombosi, T., De Zeeuw, D. L., Sokolov, I., Roussev, I., Powell, K., et al. (2005). Coronal mass ejection shock and sheath structures relevant to particle acceleration. *The Astrophysical Journal*, *622*(2), 1225–1239. https://doi.org/10.1086/427768

Manchester, W. B., Gombosi, T. I., Roussev, I., Ridley, A., Zeeuw, D. L. D., Sokolov, I. V., et al. (2004). Modeling a space weather event from the sun to the earth: CME generation and interplanetary propagation. *Journal of Geophysical Research*, *109*(A2), A02107. https://doi.org/10.1029/2003JA010150

Manchester, W. B., Gombosi, T. I., Roussev, I., Zeeuw, D. L. D., Sokolov, I. V., Powell, K. G., et al. (2004). Three-dimensional MHD simulation of a flux rope driven CME. *Journal of Geophysical Research*, *109*(A1), A01102. https://doi.org/10.1029/2002JA009672

Manchester, W. B., Kozyra, J. U., Lepri, S. T., & Lavraud, B. (2014). Simulation of magnetic cloud erosion during propagation. *Journal of Geophysical Research: Space Physics*, *119*(7), 5449–5464. https://doi.org/10.1002/2014JA019882

Manchester, W. B., Ridley, A. J., Gombosi, T. I., & DeZeeuw, D. L. (2006). Modeling the sun-to-earth propagation of a very fast CME. *Advances in Space Research*, *38*(2), 253–262. https://doi.org/10.1016/j.asr.2005.09.044

Manchester, W. B., & van der Holst, B. (2017). The interaction of coronal mass ejections with Alfvénic turbulence. *Journal of Physics: Conference Series*, *900*, 012015. https://doi.org/10.1088/1742-6596/900/1/012015

Manchester, W. B., van der Holst, B., & Lavraud, B. (2014). Flux rope evolution in interplanetary coronal mass ejections: The 13 May 2005 event. *Plasma Physics and Controlled Fusion*, *56*(6), 1–11.

Manchester, W. B., van der Holst, B., Toth, G., & Gombosi, T. (2012). The coupled evolution of electrons and ions in coronal mass ejection-driven shocks. *The Astrophysical Journal*, *756*(1), 81. https://doi.org/10.1088/0004-637x/756/1/81

Manchester, W. B., Vourlidas, A., Toth, G., Lugaz, N., Roussev, I. I., Sokolov, I. V., et al. (2008). Three-dimensional MHD simulation of the 2003 October 28 coronal mass ejection: Comparison with LASCO coronagraph observations. *The Astrophysical Journal*, *684*(2), 1448–1460. https://doi.org/10.1086/590231

Marsh, M. S., Dalla, S., Dierckxsens, M., Laitinen, T., & Crosby, N. B. (2015). SPARX: A modeling system for solar energetic particle radiation space weather forecasting. *Space Weather*, *13*(6), 386–394. https://doi.org/10.1002/2014sw001120

Mays, M. L., Thompson, B. J., Jian, L. K., Colaninno, R. C., Odstrcil, D., Möstl, C., et al. (2015). Propagation of the 7 January 2014 CME and resulting geomagnetic non-event. *The Astrophysical Journal*, *812*(2), 145. https://doi.org/10.1088/0004-637X/812/2/145

Mishev, A. L., Kocharov, L. G., & Usoskin, I. G. (2014). Analysis of the ground level enhancement on 17 May 2012 using data from the global neutron monitor network. *Journal of Geophysical Research Space Physics*, *119*(2), 670–679. https://doi.org/10.1002/2013JA019253

Möstl, C., Rollett, T., Frahm, R. A., Liu, Y. D., Long, D. M., Colaninno, R. C., et al. (2015). Strong coronal channelling and interplanetary evolution of a solar storm up to Earth and Mars. *Nature Communications*, *6*(1), 7135. https://doi.org/10.1038/ncomms8135

Nunez, M. (2011). Predicting solar energetic proton events (E > 10 MeV). *Space Weather*, *9*(7), S07003. https://doi.org/10.1029/2010sw000640

Núñez, M. (2015). Real-time prediction of the occurrence and intensity of the first hours of >100 MeV solar energetic proton events. *Space Weather*, *13*(11), 807–819. https://doi.org/10.1002/2015sw001256

Palmerio, E., Luhmann, J. G., Mays, M. L., Caplan, R. M., Lario, D., Richardson, I. G., et al. (2024). Improved modelling of SEP event onset within the WSA–Enlil–SEPMOD framework. *Journal of Space Weather and Space Climate*, *14*, 3. https://doi.org/10.1051/swsc/2024001

Papaioannou, A., Anastasiadis, A., Sandberg, I., Georgoulis, M. K., Tsiropoula, G., Tziotziou, K., et al. (2015). A novel forecasting system for solar particle events and flares (FORSPEF). *Journal of Physics: Conference Series*, *632*(1), 012075. https://doi.org/10.1088/1742-6596/632/1/012075

Park, E., Moon, Y.-J., Shin, S., Yi, K., Lim, D., Lee, H., & Shin, G. (2018). Application of the deep convolutional neural network to the forecast of solar flare occurrence using full-disk solar magnetograms. *The Astrophysical Journal*, *869*(2), 91. https://doi.org/10.3847/1538-4357/aaed40

Patsourakos, S., Georgoulis, M. K., Vourlidas, A., Nindos, A., Sarris, T., Anagnostopoulos, G., et al. (2016). The major geoeffective solar eruptions of 2012 March 7: Comprehensive sun-to-earth analysis. *Acta Pathologica Japonica*, *817*(1), 14. https://doi.org/10.3847/0004-637X/817/1/14

Posner, A. (2007). Up to 1-hour forecasting of radiation hazards from solar energetic ion events with relativistic electrons. *Space Weather*, *5*(5), 1–28. https://doi.org/10.1029/2006sw000268

Qin, G., Zhang, M., & Dwyer, J. R. (2006). Effect of adiabatic cooling on the fitted parallel mean free path of solar energetic particles. *Journal of Geophysical Research*, *111*(A8), A08101. https://doi.org/10.1029/2005ja011512

Reames, D. V. (2013). The two sources of solar energetic particles. *Space Science Reviews*, *175*(1–4), 53–92. https://doi.org/10.1007/s11214-013-9958-9

Richardson, I. G., & Cane, H. V. (2010). Near-earth interplanetary coronal mass ejections during solar cycle 23 (1996–2009): Catalog and summary of properties. *Solar Physics*, *264*(1), 189–237. https://doi.org/10.1007/s11207-010-9568-6

Richardson, I. G., Mays, M. L., & Thompson, B. J. (2018). Prediction of solar energetic particle event peak proton intensity using a simple algorithm based on CME speed and direction and observations of associated solar phenomena. *Space Weather*, *16*(11), 1862–1881. https://doi.org/10.1029/2018sw002032

Richardson, I. G., von Rosenvinge, T. T., Cane, H. V., Christian, E. R., Cohen, C. M. S., Labrador, A. W., et al. (2014). >25 MeV proton events observed by the high energy Telescopes on the STEREO A and B spacecraft and/or at earth during the first seven years of the STEREO mission. *Solar Physics*, *289*(8), 3059–3107. https://doi.org/10.1007/s11207-014-0524-8

Roussev, I. I. (2008). Eruptive events in the solar atmosphere: New insights from theory and 3-D numerical modelling. *Journal of Contemporary Physics*, *49*(4), 237–254. https://doi.org/10.1080/00107510802366658

Roussev, I. I., Sokolov, I. V., Forbes, T. G., Gombosi, T. I., Lee, M. A., & Sakai, J. I. (2004). A numerical model of a coronal mass ejection: Shock development with implications for the acceleration of GeV protons. *The Astrophysical Journal Letters*, *605*(1), L73–L76. https://doi.org/10.1086/392504

Sachdeva, N., Tóth, G., Manchester, W. B., van der Holst, B., Huang, Z., Sokolov, I. V., et al. (2021). Simulating solar maximum conditions using the Alfvén wave solar atmosphere model (AWSoM). *Acta Pathologica Japonica*, *923*(2), 176. https://doi.org/10.3847/1538-4357/ac307c

Sachdeva, N., van der Holst, B., Manchester, W. B., Tóth, G., Chen, Y., Lloveras, D. G., et al. (2019). Validation of the Alfvén wave solar atmosphere model (AWSoM) with observations from the low corona to 1 au. *The Astrophysical Journal*, *887*(1), 83. https://doi.org/10.3847/1538-4357/ab4f5e

Schwadron, N. A., Townsend, L., Kozarev, K., Dayeh, M. A., Cucinotta, F., Desai, M., et al. (2010). Earth-moon-mars radiation environment module framework. *Space Weather*, *8*(10), S00E02. https://doi.org/10.1029/2009SW000523

Scolini, C., Rodriguez, L., Mierla, M., Pomoell, J., & Poedts, S. (2019). Observation-based modelling of magnetised coronal mass ejections with EUHFORIA. *Astronomy & Astrophysics*, *626*, A122. https://doi.org/10.1051/0004-6361/201935053

Shen, C., Li, G., Kong, X., Hu, J., Sun, X. D., Ding, L., et al. (2013). Compound twin coronal mass ejections in the 2012 May 17 gle event. *The Astrophysical Journal*, *763*(2), 114. https://doi.org/10.1088/0004-637X/763/2/114

Shen, C., Xu, M., Wang, Y., Chi, Y., & Luo, B. (2018). Why the shock-ICME complex structure is important: Learning from the early 2017 September CMEs. *Acta Pathologica Japonica*, *861*(1), 28. https://doi.org/10.3847/1538-4357/aac204

Shiota, D., & Kataoka, R. (2016). Magnetohydrodynamic simulation of interplanetary propagation of multiple coronal mass ejections with internal magnetic flux rope (susanoo-cme). *Space Weather*, *14*(2), 56–75. https://doi.org/10.1002/2015SW001308

Smart, D. F., & Shea, M. A. (1976). PPS76—A computerized "event mode" solar proton forecasting technique. *Journal of Atmospheric and Solar-Terrestrial Physics*, *406*, 1125.

Smart, D. F., & Shea, M. A. (1989). PPS-87: A new event oriented solar proton prediction model. *Advances in Space Research*, *9*(10), 281–284. https://doi.org/10.1016/0273-1177(89)90450-x

Smart, D. F., & Shea, M. A. (1992). Modeling the time intensity profile of solar flare generated particle fluxes in the inner heliosphere. *Advances in Space Research*, *12*(2), 303–312. https://doi.org/10.1016/0273-1177(92)90120-m

Sokolov, I. V., Roussev, I. I., Gombosi, T. I., Lee, M. A., Kóta, J., Forbes, T. G., et al. (2004). A new field line advection model for solar particle acceleration. *The Astrophysical Journal*, *616*(2), L171–L174. https://doi.org/10.1086/426812

Sokolov, I. V., van der Holst, B., Manchester, W. B., Ozturk, D. C. S., Szente, J., Taktakishvili, A., et al. (2021). Threaded-field-lines model for the low solar corona powered by the Alfvén wave turbulence. *The Astrophysical Journal*, *908*(1), 172–183. https://doi.org/10.3847/1538-4357/abc000

Sokolov, I. V., van der Holst, B., Oran, R., Downs, C., Roussev, I. I., Jin, M., et al. (2013). Magnetohydrodynamic waves and coronal heating: Unifying empirical and MHD turbulence models. *The Astrophysical Journal*, *764*(1), 23. https://doi.org/10.1088/0004-637x/764/1/23

Sokolov, I. V., Zhao, L., & Gombosi, T. I. (2022). Stream-aligned magnetohydrodynamics for solar wind simulations. *The Astrophysical Journal*, *926*(1), 102. https://doi.org/10.3847/1538-4357/ac400f

Strauss, R. D., & Fichtner, H. (2015). On aspects pertaining to the perpendicular diffusion of solar energetic particles. *Acta Pathologica Japonica*, *801*(1), 29. https://doi.org/10.1088/0004-637X/801/1/29

Tenishev, V., Shou, Y., Borovikov, D., Lee, Y., Fougere, N., Michael, A., & Combi, M. R. (2021). Application of the Monte Carlo method in modeling dusty gas, dust in plasma, and energetic ions in planetary, magnetospheric, and heliospheric environments. *Journal of Geophysical Research*, *126*(2), e2020JA028242. https://doi.org/10.1029/2020ja028242

Thakur, N., Gopalswamy, N., Xie, H., Mäkelä, P., Yashiro, S., Akiyama, S., & Davila, J. M. (2014). Ground level enhancement in the 2014 January 6 solar energetic particle event. *The Astrophysical Journal Letters*, *790*(1), L13. https://doi.org/10.1088/2041-8205/790/1/L13

Tiwari, S. K., Falconer, D. A., Moore, R. L., Venkatakrishnan, P., Winebarger, A. R., & Khazanov, I. G. (2015). Near-sun speed of CMES and the magnetic nonpotentiality of their source active regions. *Geophysical Research Letters*, *42*(14), 5702–5710. https://doi.org/10.1002/2015GL064865

Torsti, J., Valtonen, E., Lumme, M., Peltonen, P., Eronen, T., Louhola, M., et al. (1995). Energetic particle experiment ERNE. *Solar Physics*, *162*, 505–531. https://doi.org/10.1007/978-94-009-0191-9_14

van der Holst, B., Jacobs, C., & Poedts, S. (2007). Simulation of a breakout coronal mass ejection in the solar wind. *The Astrophysical Journal*, *671*(1), L77–L80. https://doi.org/10.1086/524732

van der Holst, B., Manchester, W., IV, Sokolov, I. V., Toth, G., Gombosi, T. I., DeZeeuw, D., & Cohen, O. (2009). Breakout coronal mass ejection or streamer blowout: The bugle effect. *The Astrophysical Journal*, *693*(2), 1178–1187. https://doi.org/10.1088/0004-637x/693/2/1178

van der Holst, B., Sokolov, I. V., Meng, X., Jin, M., Manchester, W. B., Toth, G., & Gombosi, T. I. (2014). Alfvén wave solar model (AWSoM): Coronal heating. *The Astrophysical Journal*, *782*(2), 81. https://doi.org/10.1088/0004-637X/782/2/81

Vemareddy, P., & Mishra, W. (2015). A full study on the sun-earth connection of an earth-directed CME magnetic flux rope. *The Astrophysical Journal*, *814*(1), 59. https://doi.org/10.1088/0004-637X/814/1/59

Vourlidas, A., Turner, D., Biesecker, D., Coster, A., Engell, A., Ho, G., et al. (2021). *Space weather science and observation gap analysis for the national aeronautics and space administration (NASA) (technical report)*. Johns Hopkins University Applied Physics Laboratory.

Wang, Y., & Qin, G. (2015). Simulations of the spatial and temporal Invariance in the spectra of gradual solar energetic particle events. *The Astrophysical Journal*, *806*(2), 252. https://doi.org/10.1088/0004-637x/806/2/252

Whitman, K., Egeland, R., Richardson, I. G., Allison, C., Quinn, P., Barzilla, J., et al. (2022). Review of solar energetic particle models. *Advances in Space Research*, *72*(12), 5161–5242. https://doi.org/10.1016/j.asr.2022.08.006

Wijsen, N., Aran, A., Sanahuja, B., Pomoell, J., & Poedts, S. (2020). The effect of drifts on the decay phase of SEP events. *Astronomy & Astrophysics*, *634*, A82. https://doi.org/10.1051/0004-6361/201937026

Wijsen, N., Aran, A., Scolini, C., Lario, D., Afanasiev, A., Vainio, R., et al. (2022). Observation-based modelling of the energetic storm particle event of 14 July 2012. *Astronomy & Astrophysics*, *659*, A187. https://doi.org/10.1051/0004-6361/202142698

Wijsen, N., Li, G., Ding, Z., Lario, D., Poedts, S., Filwett, R. J., et al. (2023). On the seed population of solar energetic particles in the inner heliosphere. *Journal of Geophysical Research: Space Physics*, *128*(3), e2022JA031203. https://doi.org/10.1029/2022JA031203

Young, M. A., Schwadron, N. A., Gorby, M., Linker, J., Caplan, R. M., Downs, C., et al. (2020). Energetic proton propagation and acceleration simulated for the bastille day event of July 14, 2000. *The Astrophysical Journal*, *909*(2), 160. https://doi.org/10.3847/1538-4357/abdf5f

Zhang, M., & Zhao, L. (2017). Precipitation and release of solar energetic particles from the solar coronal magnetic field. *The Astrophysical Journal*, *846*(2), 107. https://doi.org/10.3847/1538-4357/aa86a8

Zhao, L. (2023a). Clear space weather center of excellence: All-clear solar energetic particle prediction. Retrieved from https://arxiv.org/abs/2310.14677

Zhao, L. (2023b). Solar wind with field lines and energetic particles (sofie) model: Application to historical solar energetic particle events [Dataset]. *University of Michigan*. https://doi.org/10.7302/fpw3-pr89

Zhao, L., & Li, G. (2014). Particle acceleration at a pair of parallel shocks near the Sun. *Journal of Geophysical Research: Space Physics*, *119*(8), 6106–6119. https://doi.org/10.1002/2014ja020103

Zhao, L., Li, G., Zhang, M., Wang, L., Moradi, A., & Effenberger, F. (2019). Statistical analysis of interplanetary magnetic field path lengths from solar energetic electron events observed by wind. *The Astrophysical Journal*, *878*(2), 107. https://doi.org/10.3847/1538-4357/ab2041

Zhao, L., Zhang, M., & Rassoul, H. K. (2016). Double power laws in the event-integrated solar energetic particle spectrum. *The Astrophysical Journal*, *821*(1), 62. https://doi.org/10.3847/0004-637x/821/1/62

Zhao, L., Zhang, M., & Rassoul, H. K. (2017). The effects of interplanetary transport in the event-intergrated solar energetic particle spectra. *The Astrophysical Journal*, *836*(1), 1–10. https://doi.org/10.3847/1538-4357/836/1/31

Zhu, B., Liu, Y. D., Kwon, R.-Y., Jin, M., Lee, L. C., & Xu, X. (2021). Shock properties and associated characteristics of solar energetic particles in the 2017 September 10 ground-level enhancement event. *The Astrophysical Journal*, *921*(1), 26. https://doi.org/10.3847/1538-4357/ac106b